AD-A107 592   CARNEGIE-MELLON UNIV PITTSBURGH PA DEPT OF ELECTRICA--ETC   F/G 17/7
OPTICAL DATA PROCESSING FOR MISSILE GUIDANCE.(U)
OCT 81   D CASASENT   AFOSR-79-0091
UNCLASSIFIED   AFOSR-TR-81-0730   NL

1 of 1
AD
A107592

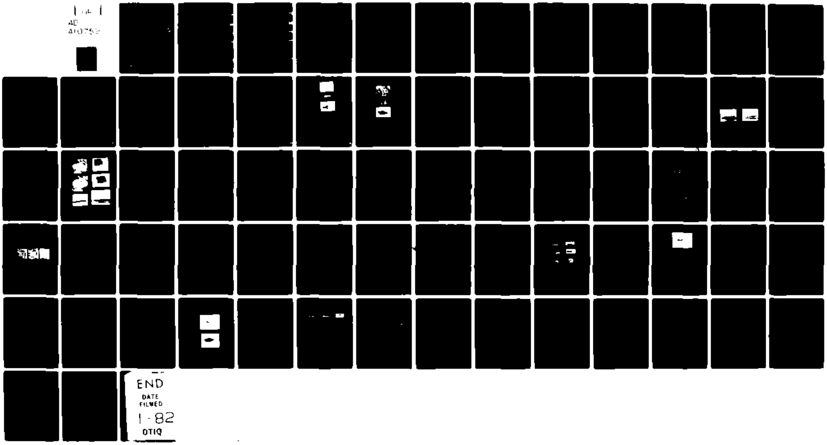

END
DATE
FILMED
1-82
DTIC

AFOSR-TR- 81 -0730

LEVEL II

(4)

AD A107592

OPTICAL DATA PROCESSING FOR MISSILE GUIDANCE

by

David Casasent
(Principal Investigator)

Carnegie-Mellon University
Department of Electrical Engineering
Pittsburgh, Pennsylvania 15213

DTIC
ELECTE
NOV 20 1981
H

Prepared for

AFOSR/NE
Building 410
Bolling Air Force Base
Washington, D.C. 20332

Attention: Dr. John Neff

AFOSR Annual Report on
Contract AFOSR 79-0091

Period Covered (1 October 1980 - 31 September 1981)

Date: 1 October 1981

DTIC FILE COPY

81 11 3

Approved for public release;
distribution unlimited.

Unclassified 1 October 1981
SECURITY CLASSIFICATION OF THIS PAGE (When Data Entered)

REPORT DOCUMENTATION PAGE

READ INSTRUCTIONS BEFORE COMPLETING FORM

1. REPORT NUMBER AFOSR-TR- 81 -0730	2. GOVT ACCESSION NO. AD-A107592	3. RECIPIENT'S CATALOG NUMBER
4. TITLE (and Subtitle) OPTICAL DATA PROCESSING FOR MISSILE GUIDANCE		5. TYPE OF REPORT & PERIOD COVERED Annual September 1980-October 1981
		6. PERFORMING ORG. REPORT NUMBER
7. AUTHOR(s) David Casasent		8. CONTRACT OR GRANT NUMBER(s) AFOSR-79-0091
9. PERFORMING ORGANIZATION NAME AND ADDRESS Carnegie-Mellon University, Department of Electrical Engineering, Pittsburgh, Pennsylvania 15213		10. PROGRAM ELEMENT, PROJECT, TASK AREA & WORK UNIT NUMBERS 61102F 2305/B2
11. CONTROLLING OFFICE NAME AND ADDRESS AFOSR/NE Building 410 Bolling Air Force Base, Washington, D.C. 20332		12. REPORT DATE 1 October 1980
		13. NUMBER OF PAGES 67
14. MONITORING AGENCY NAME & ADDRESS(if different from Controlling Office)		15. SECURITY CLASS. (of this report) Unclassified
		15a. DECLASSIFICATION/DOWNGRADING SCHEDULE N/A

16. DISTRIBUTION STATEMENT (of this Report)

Approved for public release;
distribution unlimited.

17. DISTRIBUTION STATEMENT (of the abstract entered in Block 20, if different from Report)

18. SUPPLEMENTARY NOTES

None

19. KEY WORDS (Continue on reverse side if necessary and identify by block number)

Holographic optical elements, pattern recognition, synthetic discriminant functions, multi-sensor pattern recognition.

20. ABSTRACT (Continue on reverse side if necessary and identify by block number)

The initial phase of our synthetic discriminant function optical pattern recognition research has been completed. This hyperspace description allows the use of off-line synthesis of a filter function that provides both intra-class recognition (of a key object independent of geometrical distortions) and inter-class discrimination (of a key object from candidate false targets).

A new theoretical model for multi-sensor data, a description of a general multi-sensor processor and a statistical analysis of both have also been completed.

DD FORM 1 JAN 73 1473 EDITION OF 1 NOV 65 IS OBSOLETE

Unclassified 1 October 1981
SECURITY CLASSIFICATION OF THIS PAGE (When Data Entered)

Initial experimental correlations were obtained and found to be in agreement with our model and theoretical analysis. A new parameter, the correlation measure, was found to be of use in determining the multi-sensor nature of input imagery and a |GRAD| digital preprocessing operator was found to be quite adequate for the cases considered.

Our initial optical correlations on the autonomous terminal homing data base were also completed. In this research, aperture correlation effects were overcome by a new technique, optical and digital correlations on the same data base were obtained and compared (with a high pass filter model for the optical matched filter found to be adequate and appropriate for many applications), and sensed/synthetic optical image correlations were obtained (with the help of photoreduced imagery and advanced preprocessing operations).

(4)

ABSTRACT

The initial phase of our synthetic discriminant function optical pattern recognition research has been completed. This hyperspace description allows the use of off-line synthesis of a filter function that provides both intra-class recognition (of a key object independent of geometrical distortions) and inter-class discrimination (of a key object from candidate false targets).

A new theoretical model for multi-sensor data, a description of a general multi-sensor processor and a statistical analysis of both have also been completed. Initial experimental correlations were obtained and found to be in agreement with our model and theoretical analysis. A new parameter, the correlation measure, was found to be of use in determining the multi-sensor nature of input imagery and a |GRAD| digital preprocessing operator was found to be quite adequate for the cases considered.

Our initial optical correlations on the autonomous terminal homing data base were also completed. In this research, aperture correlation effects were overcome by a new technique, optical and digital correlations on the same data base were obtained and compared (with a high pass filter model for the optical matched filter found to be adequate and appropriate for many applications), and sensed/synthetic optical image correlations were obtained (with the help of photoreduced imagery and advanced preprocessing operations).

AIR FORCE OFFICE OF SCIENTIFIC RESEARCH (AFSC)
NOTICE OF TRANSMITTAL TO DTIC
This [illegible] reviewed and is
[illegible] AFR 190-12.
Distr[illegible] unlimited.
MATTHEW J. [illegible]
Chief, Technical Information Division

1. INTRODUCTION

During the past year, our research in optical data processing for missile guidance has addressed various new algorithms, system architectures, component tests, and analyses of various image data bases. As in the past years, we have been quite faithful in reporting our AFOSR sponsored research in various journal and conference publications. Copies of the more relevant of these papers are thus included as the chapters of this report to provide concise documentation of our work.

In Section 2, we provide a summary and overview of our research progress made in the past year. Details on the more salient topics are provided in Sections 3 - 7. In Section 9, we enumerate our AFOSR sponsored publications and the presentations given on this research in the past year.

Accession For
NTIS GRA&I ☑
DTIC TAB ☐
Unannounced ☐
Justification
By
Distribution/
Availability Codes
Avail and/or
Dist Special
A

2. SUMMARY AND OVERVIEW

2.1 AIRBORNE OPTICAL CORRELATOR (Section 3)

Since the intended application for most of our pattern recognition techniques is missile guidance, attention to the components for use in such a system is necessary together with a rugged and stable system architecture. In [1], we first addressed this subject. In [2] and [3], we provided additional details of this work. In [4] (Section 3), we summarize these results with attention to: the use of laser diode sources (rather than the larger laser sources used in the conventional laboratory optical system), holographic optical elements (rather than the larger and heavier conventional glass lenses), plus a new architecture (the lensless matched spatial filter) with greatly improved stability and ruggedness.

The basic system architecture involves imaging the laser diode source onto a lensless matched filter with the input placed behind the lens. The lensless matched filter is a combined matched filter and holographic optical element (formed with a converging reference beam, rather than the conventional plane wave reference beam normally used). When part of the input scene contains the reference object, a focused beam emerges from the matched spatial filter and self focuses on the output correlation plane. Since the second Fourier transform lens and the matched spatial filter are recorded on the same plate, the positioning tolerances between these two components are inherently satisfied. This greatly simplifies the stability and ruggedness of the resultant system. The matched spatial filter is formed in visible light at one wavelength λ_1 (for which spectroscopic grade film of adequate sensitivity is available), whereas correlation is performed with a laser diode source at a second wavelength λ_2. The architecture of the scaling correlator system used is adjusted to correct for different recording and reading wavelengths.

Our present work (Section 3) has included an analysis of the spatial and temporal coherence of the laser diode source and the shift invariance and aberrations of the holographic optical elements used. Future work in this area is anticipated and will be reported upon in future annual reports. The general philosophy used in our lensless matched spatial filter correlator will be pursued in our future work (i.e. alterations of the standard optical processor architectures, when non-conventional components, such as holographic elements, or laser diodes, are employed).

2.2 SPATIAL LIGHT MODULATORS

A vital feature of most optical data processing systems is the real time and reuseable 2-D spatial light modulator necessary to input data to the optical processor. During the past year, we have performed a test and evaluation of five Soviet From and Priz light modulators. The results of this phase of our research were most attractive and will be presented later when available [5-8].

2.3 OPTICAL EXPERIMENTS FOR AUTONOMOUS TERMINAL HOMING (Section 4)

The major image data base presently available is the autonomous terminal homing DARPA set. We have completed our initial pattern recognition analysis on this data base (Section 4) [9]. The optical system architecture used was a weighted matched spatial filter correlator. The low resolution and modulation of this data base introduced a new problem (the dominance of aperture correlations over image correlations), which we overcame by the use of different apertures during synthesis of the matched spatial filter and during correlation with the on-line sensed image. In this study, we also provided the first direct comparison of optically and digitally correlated data (with various digital preprocessing operations used). From these tests, we found that a highpass filter model was quite appropriate for an optical weighted matched spatial filter correlator. The experiments were performed on multi-sensor data and from comparative results obtained with different preprocessing operators, we found that a simple highpass filtering preprocessing operator was often adequate. For more true multi-sensor data with a small correlation measure (see Section 5), the |GRAD| operator (obtained by digital preprocessing) was preferable.

The final feature of this research was our first successful optical correlations on sensed input imagery and synthetic reference data. As our work showed, such correlations were possible only when aperture effects were removed, when the input imagery was photoreduced, and when advanced preprocessing operators (e.g. gray tone modification and small surface lysing) were applied to the data bases.

Analysis of this data base and more attention to different preprocessing operators is required and will be the subject of future work by us.

2.4 MULTISENSOR PATTERN RECOGNITION (Section 5)

A major class of imagery on which considerable pattern recognition research has been performed is multi-sensor data. In [10], we described a new statistical model for multi-sensor imagery and a general multi-sensor processor. We performed a a statistical analysis of our general processor using our image model. In [11] (Section 5), we describe our recent results in which experimental verification of our model and processor were obtained. These tests verified the use of our new parameter (the correlation measure) as a measure of whether the image pairs were unisensor or multi-sensor imagery. These tests also concentrated upon the use of and need for various preprocessing operators in the correlation (for acquisition) of multi-sensor data.

For image pairs with high correlation measures, the data was found to be uni-sensor and a highpass filter preprocessing operator was adequate. For data with low (< 0.5) correlation measures, a nonlinear magnitude operator provided improved results. We also found the |GRAD| operator to well approximate whitening, edge enhancement and polarity equilization. The use of histogram reshaping as a preprocessing operator was found to provide a 6-32% improvement for different multi-sensor image sets. As the number of objects in the image was increased, we found the data to more closely approach multi-sensor imagery. Our theoretical threshold values were also found to be verified by experiment. During the next year, we will more completely document and analyze these initial results.

2.5 INTRA-CLASS PATTERN RECOGNITION USING SYNTHETIC DISCRIMINANT FUNCTIONS (Section 6)

Maintaining pattern recognition in the face of geometrical distortions between the input and reference data (especially 3-D aspect angle differences) is perhaps one of the most difficult data processing problems in existence. To address this problem, we suggested [12] the use of a hyperspace formulation of the data for the problem in which each input image is represented by a vector point in a hyperspace. Our initial technique has been refined in [13] (Section 6) to include a new maximum common information concept and the use of other basis function synthesis techniques. This approach allows a synthetic discriminant function (defined by a linear combination of the image training set) to be produced off-line and to be subsequently used in the future recognition of the same target independent of its geometrical aspect.

Although our initial results are most promising, much additional work is necessary on this concept. We intend to extensively pursue this concept during the coming years.

2.6 INTER-CLASS DISCRIMINATION USING SYNTHETIC DISCRIMINANT FUNCTIONS (Section 7)

As an initial extension of our synthetic discriminant function research (Section 6), we considered the case of discrimination in the two-class pattern recognition problem and suggested several new techniques and provided initial experimental verification of them [14] (Section 7). These concepts included: maximum common information filters, multi-channel filters, non-unitary transformations, and decorrelation transformations. Extensive additional research on this aspect of the synthetic discriminant function concept with attention to multi-class pattern recognition problems and statistical filters is the subject of current research that will be reported upon in future annual reports.

2.7 ITERATIVE OPTICAL PROCESSOR

Due to cancellation of other support for our iterative optical processor [15] research, interim temporary funding of this project by AFOSR has enabled us to complete a Ph.D thesis in this area, to generalize on the different applications possible for this optical system architecture [16], and to document our work in this area [17-19]. We will detail and highlight this phase of our research in our next annual report (after publications on the subject are finalized).

2.8 FUTURE RESEARCH DIRECTION

Our future research is expected to follow the major lines addressed in the past two years (real-time devices, optical system components and airborne processors) with major attention given to new pattern recognition architectures and algorithms (especially hybrid optical/digital systems). As can be seen, the flavoring of our recent and future research is being directed toward more use of statistical analysis and digital simulation of optical systems. We will also continue to apply our new algorithms, architectures and concepts to new missile guidance image data bases. Several general pattern recognition reviews were published during the past year under AFOSR support and may be useful for a general review of this area [20-23].

SECTION 3

STABLE AND COMPACT AIRBORNE OPTICAL PATTERN RECOGNITION SYSTEM CONCEPT

A LASER DIODE/LENSLESS MSF OPTICAL PATTERN RECOGNITION SYSTEM

by

D. Casasent, M. Shen*, F. Caimi, T. Luu and B. Feng*
Carnegie-Mellon University
Department of Electrical Engineering
Pittsburgh, Pennsylvania 15213

ABSTRACT

A compact and rugged optical correlator is described that uses a laser diode source and holographic optical elements. Use of a lensless matched spatial filter, and corrections for wavelength scaling and aberration errors plus an analysis of the system's shift invariance are included.

1. INTRODUCTION

Optical Pattern recognition (OPR) by matched spatial filter (MSF) correlation is well-known [1]. The advent of holographic optical elements (HOEs) [2-3], laser diode sources and new architectures has made rugged and compact OPR systems most attractive [4-7] for commercial and airborne applications. In this paper we describe the first system [7] to employ both solid-state sources and HOEs. A lensless MSF in which the MSF and second Fourier transform (FT) lens are combined on one plate [8-9] was used to avoid critical alignment of these two components. The design, experimental verification and shift invariance of this system are discussed in Sect. 2. When a laser diode source is used, the MSF is recorded at one wavelength and correlation is performed at a second wavelength. A new scaling correlator topology using an imaging lens was employed to correct for wavelength changes. The design, fabrication, aberration analysis and experimental demonstration of the system are presented in Sect. 3.

2. LENSLESS MSF

2.1 THEORY

The system used to record a lensless MSF in shown in Fig. 1. It it similar to the conventional technique [1] except that a converging reference beam is used rather than a plane wave. For simplicity of notation, only a 1-D analysis is included with no loss of generality. During MSF synthesis, $h(x)$ is placed at P_1 and its FT incident on P_2 is $u_s(x_2) = H(x_2/\lambda f_L)$. The spatial coordinates of P_1, P_2, and P_3 are denoted by x_1, x_2, and x_3 respectively; λ is the wavelength of the incident light and f_L is the focal length of lens L_1. The converging reference beam at P_2 is described by

$$u_r(x_2) = \exp[-jk(x_0-x_2)^2/2z], \tag{1}$$

where $k = 2\pi/\lambda$, x_0 is the distance from the axis in P_3 at which the converging beam focuses, and z is the orthogonal distance from P_2 to P_3. The pattern recorded at P_2 is $|u_s+u_r|^2$. We assume that the transmittance of P_2 after development is equal to the incident exposure and thus the term of interest in this MSF at P_2 is

$$u_t(x_2) = H^*(x_2/\lambda f_L)\exp[-jk(x_0-x_2)^2/2z], \tag{2}$$

where the constant phase factor describing its propagation direction is omitted for simplicity.

If P_2 is re-illuminated with u_s, a point of light appears at $x_3 = x_0$. Our major concern is that this occurs without the need for a second FT lens between P_2 and P_3. Thus no critical alignment of these components is needed in this lensless MSF system. If h is shifted in P_1 during reconstruction, the locationof the point of light in P_3 should shift from its original x_0 location by an amount proportional to the shift of h in P_1. This shift invariance is required in pattern recognition.

To see the use of such a system for pattern recognition, we place $f(x_1) = h(x_1+\epsilon) + g(x_1)$ at P_1. This function contains the reference $h(x_1)$ displaced from the origin by an amount ϵ and $g(x_1)$ denotes the rest of the input. We assume $g \circledast h = 0$ and describe the light distribution incident on P_2 for the term of interest by

---

*Visiting Scholars from Chengdu Institute of Optics and Electronics, People's Republic of China.

$$u_2(x_2) = H(x_2/\lambda f_L)\exp(jkx_2\varepsilon/f_L). \tag{3}$$

Leaving P_2, we have (suppressing constant phase terms for simplicity)

$$u_2(x_2)u_t(x_2) = H(x_2/\lambda f_L)H^*(x_2/\lambda f_L)\exp(-jkx_2^2/2z)\exp[jkx_2(\varepsilon/f_L+x_0/z)]. \tag{4}$$

At P_3 we find the FT of (4) or (omitting a quadratic phase factor, that is negligible when intensity is detected at P_3)

$$u_3(x_3) = h(x_3f_L/z) \circledast h(x_3f_L/z)*\delta(x_3+x_0+\varepsilon z/f_L). \tag{5}$$

Inspection of (5) shows that this P_3 pattern is the correlation of h displaced from the reference point x_0 by an amount $z\varepsilon/f_L$ proportional to the displacement ε of h from the center of P_1.

Many authors have proposed (and some have used) convergent reference beams for diverse purposes [8, 9, 11-13]. In our work, we are concerned with the aberration effects of the HOE on the system's shift invariance as well as the use of the system for pattern recognition [14].

2.2 EXPERIMENTS

The system of Fig. 1 was assembled using: $\lambda = 633$ nm, $f_L = 500$ mm, $\theta = 11.3°$ and $x_0 = 78$ mm. The input function f used is shown in Fig. 2a. It contains four occurrences of the key word "PROFESSOR", which we select as our reference function h (Fig. 2b). A lensless MSF of this function h was produced at P_2, f was placed at P_1 and the output correlation plane pattern in the vicinity of $(x_3, y_3) = (x_0,0)$ in P_3 appeared as shown in Fig. 2c on an isometric display [14]. The locations of the four correlation peaks are seen to correspond to the four positions of the reference word in the full input image.

2.3 ANALYSIS

A feature of this and any MSF system for OPR is proper selection of the beam balance ratio $K = |u_r/u_s|^2$ used during MSF synthesis [10]. Since u_s varies spatially, so does K. Since the modulation of the MSF is a maximum when $K = 1$, we can select the spatial frequency band in which to set $K = 1$ and hence enhance certain spatial frequencies in the input data during MSF synthesis. We refer to this as weighted MSF synthesis [10]. For the input text data of Fig. 2a, the FT of the word "PROFESSOR" was found to exhibit peaks at spatial frequencies corresponding to the reciprocal of the: stroke width, spacing between letters, the width of a letter and half the height of a letter. The FT information in the word is present as modulation about these spatial frequencies [15]. The latter two spatial frequencies (letter width and half-letter height) coincide at 3.7 cy/mm, where a bright FT plane spot is observed. We adjusted K to be one at this spatial frequency during synthesis of the MSF and thus maximized the correlator's performance. Such an MSF acts as a bandpass filter centered at 3.7 cy/mm. Because of this, the HOE need only operate over a band of spatial frequencies and thus its performance is less demanding than that of the normal FT or HOE lens.

We now consider the effect of weighted MSF synthesis on HOE aberrations and the system's shift invariance. Particular attention is given to astigmatic aberrations [9, 16]. Including third order aberrations, denoting the field angle of the key object by $\tan\beta = \varepsilon/f_L$ and assuming $\tan\beta \ll 2x_0/R_0$, where R_0 is the distance from the center of P_2 to $x_3 = x_0$, we find the optical path difference for the system to be $\Delta r_a \simeq x_2^2x_0(\tan\beta)/R_0^2$ and $(\tan\beta)_{max} = D/2f_L$, where D is the input aperture. If the maximum input spatial frequency is f_m, the maximum optical path difference error is

$$\Delta r_{a\ max} = f_m^2\lambda^2Df_L\sin\theta/2R_0, \tag{6}$$

where $\sin\theta = x_0/R_0$. In the design of our experimental system, we restricted f_m and D, minimized θ and f_L, and increased R_0 to reduce (6). From [16], the astigmatic phase aberration ϕ_a expression was found. A quadratic phase error model was assumed. From [17] the loss ρ in the correlation peak intensity I_p was found to be related to the standard deviation δ_ϕ of ϕ_a over the full aperture by

$$p = 1-\delta_\phi^2. \tag{7}$$

Inserting system values into (7), a plot of p for input displacements Δx, from +10 mm to -10 mm was made. From this theoretical curve, a maximum I_p variation of only 20% was predicted for ±10 mm displacements of h(x) across the full input aperture. The nearly uniform values for the four correlation peaks in Fig. 2c verifies the excellent shift-invariance of this system design. Detailed experimental measurements of I_p were made for ±10 mm input displacements and a maximum I_p loss of only 10% (or half the theoretically predicted value) was found. The superiority of the experimental data to the theoretical predictions is attributed to the bandpass effects of the weighted MSF. Recall that the above theory assumed that the HOE aberrations existed over the entire spatial frequency aperture of the HOE. Thus weighted MSF synthesis [10] reduces HOE aberration effects and makes the design of a shift-invariant lensless MSF correlator with low 10% variations in I_p realistic [14].

3. LASER DIODE CORRELATOR

When a laser diode at λ_2 is used as the light source during correlation, its typical λ_2 value is not in the wavelength range of MSF media. Thus the lensless HOE/MSF at P_2 must be synthesized off-line at λ_1 and correlation performed at the different λ_2 of the laser diode. This $\mu = \lambda_2/\lambda_1$ wavelength change is equivalent to a scale error in the imagery. In this section, we discuss this aspect of laser diode correlators and other laser diode parameters and their effects on the system's design and performance.

3.1 WAVELENGTH-SCALING CORRELATOR

The laser diode correlator used is shown schematically in Fig. 3. During MSF synthesis, L_1 is illuminated with a plane wave at λ_1 and the converging reference beam is used. With P_1 placed behind L_1, the FT of the P_1 data is scaled [18] by f_L/d. By varying d, the scale change μ can be compensated. To satisfy the focusing conditions, the scale change must be kept below 20% [10]. We denote the distances d and e and the angle θ in Fig. 3 during MSF synthesis and correlation by subscripts 1 and 2. To compensate for the scale change μ and to satisfy focusing conditions, we must satisfy $d_2 = d_1/\mu$, $e_2 = e_1/\mu$ and $\sin\theta_1 = \mu\sin\theta_2$. The displacement Δx_3 of the output correlation is related to the displacement Δx_1 of the input by $\Delta x_3/\Delta x_1 = e_2/d_2 = e_1/d_1$. By choosing $\Delta x_1 << d_2$ and $\Delta x_3 << e_2$, field angles and hence distortion effects will be small and HOE aberration effects will be minimized.

Such a wavelength-scaled correlator was assembled and tested [19] using gas lasers (λ_1 = 488 nm Argon laser, λ_2 = 633 nm He-Ne laser). Less than 10% variation in I_p were observed for ±10 mm input displacements. A system with HOE elements for both L_1 and L_2 was also assembled and correlations were successfully performed with gas laser sources [19]. Although the output light level was low due to the low diffraction efficiency of the HOE elements, acceptable output correlations were obtained. Better results are possible if bleached or dichromated gelatin elements [2, 3] with higher (80% vs 3%) diffraction efficiency were used.

3.2 ABERRATION ANALYSIS

For the laser diode correlator, we use λ_1 = 633 nm and λ_2 = 794.5 nm (Mitsubishi ML-4001 laser diode). The astigmatic aberration equation of [16], in our notation, becomes

$$W_a = (x_m^2/2\lambda_2)[(\mu^3-\mu)x_0^2/e_1^3 + 2\mu^3x_0\Delta x_1/e_1^2d_1 + (\mu^3\Delta x_1^2/d_1^2)(1/e_1 - 1/d_1)]. \tag{8}$$

The system parameters chosen for our correlator of Fig. 3 were: $e_1 = d_1$ = 400 mm, f_{L1} = 760 mm, f_m = 10 cy/mm, x_m = 2.5 mm, Δx_1 = 12.5 mm and x_0 = 100 mm. For these values, we find $W_{a\,max} = 0.44\,\lambda_2$ and $W_{a\,rms} = 0.13\,\lambda_2$. These low phase errors should result in a high performance correlator. Recall that weighted MSF synthesis will reduce these W_a effects even more.

3.3 LASER DIODE EFFECTS

The temporal coherence of a laser diode varies with power and temperature and can result in a source width $\Delta\lambda_2$ and/or a wavelength shift $\Delta\lambda_2$. For the laser diode used, $\Delta\lambda_2 = 0.2$ nm and $\Delta\lambda_2' = 2$nm. For our case $N \lesssim \lambda_2/\Delta\lambda_2' = 400$. We expect the system to operate well for higher N because most of the contribution to the correlation is due to spatial frequency data below the maximum and the above result thus gives a quite worst-case limit on N. The spectral spread $\Delta\lambda_2$ of the source will produce a divergence $\Delta\theta_2$ in the wavefront leaving P_2 during correlation. This can affect the shape and I_p value of the correlation. To reduce this effect, we require [5, 7]

$$\Delta\lambda_2 \lesssim \lambda_2^2/(2\mu x_m \sin\theta_1). \tag{9}$$

For our system, $\sin\theta_1 = 0.25$, $\mu = 1.26$ and thus satisfying (9) requires $\Delta\lambda_2 \lesssim 0.4$ nm. Since the $\Delta\lambda_2$ of our laser diode source is half of this value, we expect no problems from this error source (with our selected system design). Only $\Delta\lambda_2$ not $\Delta\lambda_2'$ affects the shape of the correlation whereas the larger of $\Delta\lambda_2$ and $\Delta\lambda_2'$ affects N, the space bandwidth of the input in 1-D.

The spatial coherence of the laser diode source used was also considered. This parameter was obtained from fringe visibility measurements. Over a 25 mm input aperture, V was a minimum of 0.75. From [20], we define V as the ratio of coherent intensity I_c to total intensity I_t. Assuming uniform illumination at P_1 and since the correlator's output is due to the coherent light contribution, we expect the correlation peak intensity I_p to be proportional to the square of I_c. We thus expect correlation I_p and SNR to be decreased by a factor V^2 due to the limited ($V \neq 1$) spatial coherence of the laser diode used. For our system, the source's spatial coherence will cause only a 2.5 dB loss in SNR as the input object shifts from the center to the edge of the P_1 aperture. This is again a worst-case result, for reasons similar to those noted earlier.

Proper collimation of the laser diode source should also be insured. For $2u = 10°$ aperture angle of the laser diode (see Fig. 7) and its wavelength, the source can be considered to be a point. We can thus use a simple imaging optical lens for L_1 with quite modest requirements (a cemented doublet suffices). A trade off exists between uniformity of the illumination at P_1 (by increasing the distance from the laser diode to L_1) and less light power in the P_1 aperture (shorter distance from the source to P_1). For the system design used, L_1 intercepted a 7° cone angle. For this case, one-sixth of the source light is useable and the P_1 illumination has a 30% intensity taper (thus a 3 dB variation in I_p and SNR for input displacements over the full P_1 aperture is expected, again in worst-case). These various source coherence, lens aberration, and uniform illumination effects can add in worst-case to produce I_p and SNR variations of 6 dB maximum.

3.4 EXPERIMENTS

All the above analysis issues were incorporated into the design of an experimental system in the topology of Fig. 3. In Fig. 4 we show the input, reference and output correlation plane pattern obtained with the MSF formed at $\lambda_1 = 633$ nm and correlation performed with a laser diode at $\lambda_2 = 795.4$ nm. The input transparency used was a radar image with a 24 mm x 30 mm format. The SNR of the correlation is seen to be quite good even though the reference was located at the edge of the input scene.

4. SUMMARY AND CONCLUSIONS

A low size and weight optical correlator suitable for airborne applications has been described, designed, analyzed, fabricated, tested and successfully demonstrated. The system employs holographic optical elements in a lensless MSF architecture with improved system alignment and stability features. The light source used during correlation was a laser diode. It was thus necessary to record the matched spatial filter at one wavelength and perform the correlation at the different wavelength of the laser diode. A scaling correlator architecture was used to accommodate the wavelength change and a system design requiring only a simple imaging input lens to focus the laser diode onto the filter was employed. A complete system design and analysis including aberration effects and with attention to the system's shift-invariance was performed. The experimental results obtained verified the usefulness of this system.

ACKNOWLEDGEMENTS

The support of this research by the Air Force Office of Scientific Research is gratefully acknowledged as is the support of the Chinese Academy of Sciences.

REFERENCES

1. A. Van der Lugt, IEEE, IT-10, 139 (1964).
2. B. Chang and C. Leonard, Applied Optics, 18, 2407 (1979).
3. B. Chang, Soc. Photo Instru. Engrs., 177, 71 (1979).
4. B. Guenther, et al., IEEE, QE-15, 1348 (1979).
5. J. Duthie, et al., Soc. Photo Instru. Engrs., 231 (April 1980).
6. C. Calderone, Final Report on Contract DAAK 40-77-c-0089 (17 December 1979) Grumman Aerospace Corporation.
7. F. Caimi, et al., Applied Optics 19, 2653 (1980).
8. W. Maloney, Applied Optics, 10, 2127 (1971)
9. M. Bage and M. Beddoes, Applied Optics, 15, 2830 (1976).
10. D. Casasent and A. Furman, Applied Optics, 17, 1652, 1662 (1978).
11. G. Groh, Applied Optics, 7, 1643 (1968).
12. D. Gabor, Optica Acta., 16, 519 (1969).
13. S. Ragnarsson, Phys. Ser., 2, 145 (1970).
14. M. Shen, et al., Optics Communications, 34, 311 (1980).
15. D. Casasent, et al., Optical Engr., 19, 716 (1980).
16. E. Champagne, J. Opt. Soc. Amer., 57, 51 (1967).
17. T. Luu and D. Casasent, Applied Optics, 18, 791 (1979).
18. A. Van der Lugt, Applied Optics, 5, 1760 (1966).
19. M. Shen, et al., Optics Communications, 34, 316 (1980).
20. M. Born and E. Wolf, Principles of Optics (3rd edition, 1956) p. 503-506.

FIGURES

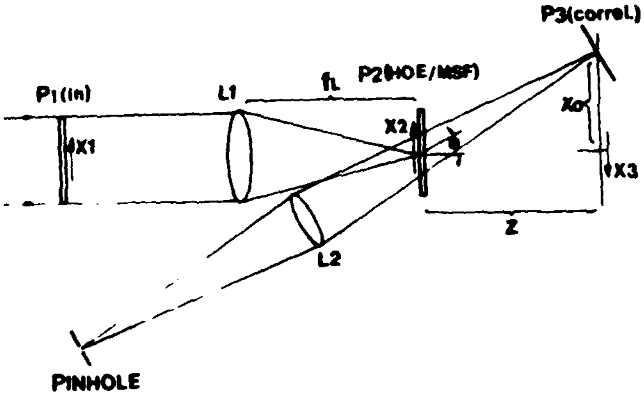

Figure 1 Schematic diagram of a lensless MSF optical correlator system [14].

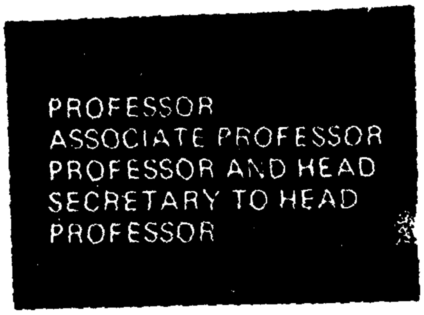
PROFESSOR
ASSOCIATE PROFESSOR
PROFESSOR AND HEAD
SECRETARY TO HEAD
PROFESSOR

(a) input

(b) reference

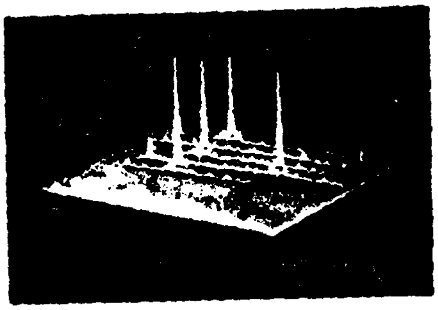

(c) output correlation

Figure 2 Optical pattern recognition performed on the system of Fig. 1, (a) input, (b) reference, (c) output correlation plane pattern for an MSF of the key word "PROFESSOR" [1-[illegible]].

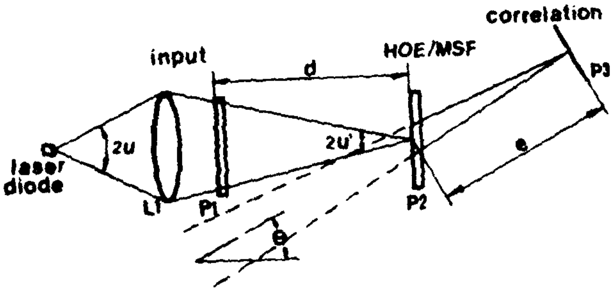
correlation
input
d
HOE/MSF
P3
2u
2u'
laser diode
L1
P1
P2
e
θ

Figure 3 Schematic diagram of a laser diode/lensless MSF correlator [7].

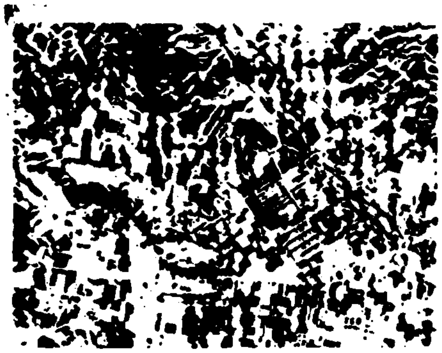

(a) input

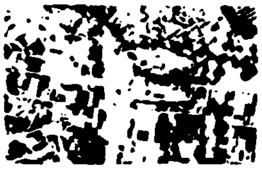

(b) reference

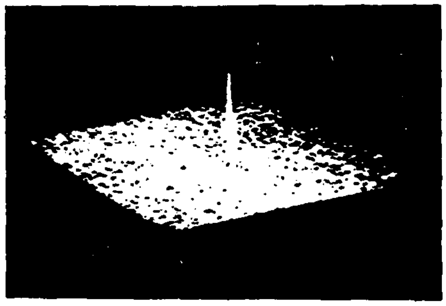

(c) output correlation

Figure 4 Experimental image pattern recognition data obtained using the system in Fig. 3, (a) input, (b) reference, (c) output correlation [7].

SECTION 4

OPTICAL PROCESSING ON THE AUTONOMOUS TERMINAL HOMING DATA BASE

310-25

IMAGE QUALITY EFFECTS IN OPTICAL CORRELATORS

David Casasent, Saulius Eiva* and B.V.K. Vijaya Kumar

Carnegie-Mellon University, Department of Electrical Engineering
Pittsburgh, Pennsylvania 15213

*Present Address: Harris Corporation, Rhode Island

ABSTRACT

Three aspects of image quality and their effects in an optical matched spatial filter correlator are described. These concern operation on: digitized imagery, data with low modulation and low space bandwidth product, and synthetic reference imagery. To address these practical problems, we employ: spatial filtering, edge enhancement, use of different apertures, photoreduced imagery, and digital preprocessed data. The first experimental data on optical matched spatial filter correlations with synthetic reference imagery and the first comparative data on digitally and optically processed multisensor image correlations are included. From these experiments, we find an optical weighted matched spatial filter correlator to be adequate for most multisensor data and that advanced digital preprocessing operators are necessary when presently available synthetic reference imagery is used.

1. INTRODUCTION

The scaling correlator version of the optical frequency plane correlator [1] (Figure 1) using weighted matched spatial filter (MSF) synthesis [2] is perhaps the most widely used optical pattern recognition system [3]. In this paper, we address how the quality of the imagery used in such an optical system affects the processors performance. The data bases we used include multisensor imagery and imagery with synthetic reference functions. These data are part of the DARPA autonomous terminal homing (ATH) data base. In Section 2, we describe the optical processor and address the issues of optical processing of digitized data. A simple low pass spatial filtering aperture in the Fourier transform or matched spatial filter plane is shown to be necessary and adequate to remove the effects of correlations due to the fixed regular input pixel pattern present in such data. In Section 3, the difference between system, detector and correlation noise are specifically denoted and the importance of the system's light level budget, the system's diffraction efficiency η and the detector's sensitivity are addressed. Solutions include higher power light sources and more sensitive detectors. However preferable solutions are increased data modulation and data space bandwidth product and the use of bleached or dichromated gelatin matched filters [4].

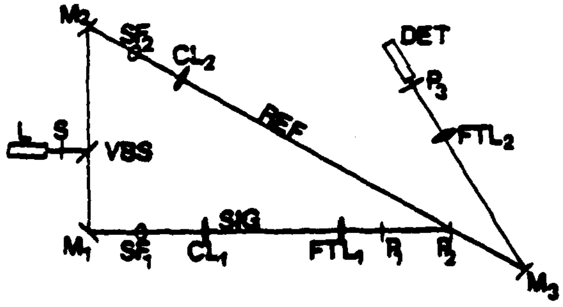

Figure 2.1 Topology of the Scaling Correlator

FIGURE 1. Schematic diagram of the expermental optical scaling frequency plane correlator used. Code: L(laser,λ=514nm); S(shutter); VBS(variable beam splitter); M(mirror); SF(pinhole spatial filter, 10X objective, 7um); CL(collimating lens, f_L= 762mm); FTL(Fourier transform lens, f_L= 762mm); P_1(input plane); P_2(MSF frequency plane); P_3(correlation plane).

Optical correlation experiments on the ATH data base clearly show that this data has quite low modulation, spatial frequency content and space bandwidth product. Fourier transform plane scans and our initial quantitative analysis in Section 4 show the magnitude of this problem. It manifests itself as a quite appreciable output correlation peak due to the input aperture with a smaller peak due to the correlation of the imagery itself. In Section 5, we advance the theory and experimental verification of a new laboratory technique that can overcome such problems. To suppress the effects of the aperture correlation, we use different

Casasent

310-25

apertures for the input and reference functions. This technique, together with the high pass filtering action of the MSF are shown to decrease the magnitude of the aperture correlations and to allow detection of the true image correlation output.

In Section 6, we consider optical correlation of multisensor ATH data. Both digital [5] and optical correlation data on the same image set are presented and compared with attention to the different preprocessing operations possible in an optical and digital system and with attention to the different preprocessing operations required for multisensor pattern recognition. We find that in most practical multisensor pattern recognition cases, the optical and digital systems perform comparably and thus conclude that in the majority of practical cases, optical processors using weighted matched spatial filter synthesis are adequate for multisensor pattern recognition.

In Section 7, we turn our attention to the ATH data base containing synthetic reference objects. These are found to differ considerably from the on-line sensed inputs that occur. In this case, more advanced preprocessing techniques are necessary to allow high quality output correlations to be obtained. Our experiments with several different digitally preprocessed data are summarized. We find the gray tone modification operator to perform the best, but note that the small surface lysing preprocessing operator requires more analysis and that more attention to modifications of both operators are needed when the number of independent objects in the target scene to be recognized increases.

2. OPTICAL PROCESSING OF DIGITIZED DATA

Much of the presently available image data bases are digitized. The ATH data base represents one of the most complete image pattern recognition data bases available. It contains sensed (real) and synthetic imagery with various differences present in the imagery within a given set. All of the sensed images have 100 rows and 150 columns, whereas the synthetic images are 150 x 150. For optical processing, these data are recorded on film (usually in a 35mm format). The resultant image data thus has fixed horizontal and vertical pixel patterns (with the vertical pattern due to the fixed scan line separation and the horizontal pattern due to the fixed pixel width). Care must be taken to remove the fixed image pixel pattern from the data, else it will produce a considerable contribution to the output correlation. In [6], we first noted this problem and found that it was easily overcome by placing an aperture in front of the MSF or frequency plane to block the spatial frequency components corresponding to the fixed horizontal and pixel spacings. Since the spatial frequency corresponding to the pixel spacing represents the highest input spatial frequency data, they can easily be filtered out without degrading the image information (which by definition must lie at a lower spatial frequency).

The optical system used in our experiments (Figure 1) employed weighted MSF synthesis [2]. This concept uses the fact that the spatial frequency portion of the data to be emphasized can be controlled by picking the spatial frequency u' at which the beam balance ratio K between the intensities of the plane wave reference beam and the signal beam equals unity. As K is adjusted to equal unity at different spatial frequencies, low, medium or high spatial frequency data in the input and reference imagery can be emphasized. We use this technique in Section 5 to perform the correlation on edge-enhanced data (to decrease the effect of aperture correlations). In Section 6, the same technique is used to approximate a highpass filter preprocessing operator for multisensor image pattern recognition. In Section 7, the same technique is again used for similar reasons on synthetic reference imagery.

Our ATH experiments reported here used two different data sets. The first (Section 6) contained imagery of the Ames building obtained with 3-4 different sensors at three different locations either downlooking (0°) or target looking (from a depression angle of 20° with respect to the normal). The second data set (Section 7) contained synthetic and sensed images of a Lockheed building. In our initial autocorrelation experiments, K was set equal to one at spatial frequencies from 0.9-15cy/mm. For cross-correlations, spatial frequencies in a lower 0.86-6.6cy/mm spatial frequency range were used. In our multisensor experiments, the $8-12\mu m$ sensed images were used as references since they correspond to a good spatial frequency band in which significant target information and passive detectors exist. This band is also compatible with present plans for the ATH system that include use of an $8-12\mu m$ passive sensor and a $10.6\mu m$ active CO_2 laser radar (for range information). The multisensor Ames image data had quite low modulation with negligible information content beyond 3cy/mm. The synthetic reference images (Sections 3 and 7) were of even lower modulation and space bandwidth product, necessitating the use of even lower spatial frequency settings below 0.64cy/mm. To allow this and to produce optical correlation plane data whose results are more in agreement with those predicted by theory, we photoreduced the sensed and synthetic image data bases and used more advanced digital preprocessing algorithms (Section 7). Our results on these data were in agreement with theory.

Casasent 2

310-25

3. NOISE SOURCES IN OPTICAL CORRELATORS

The dynamic range of a digital system is well-known to be large. But moreso, these systems can handle low modulation data by proper normalization techniques. Many practical problems that arise in optical systems can thus be ignored in digital processing such as: light source intensity levels, filter diffraction efficiency, and detector sensitivity. As our performance measure for pattern recognition, we use the output correlation SNR defined as the ratio of the intensity of the correlation peak to the spatial average of the output correlation pattern far ($\tau >> 0$) from the correlation peak (assumed to occur at $\tau = 0$). In Figure 2, we show various noise sources that are present in an optical correlator. All outputs are measured with a scanning photometric microscope with a fiber optic probe and high gain low noise PMT interfaced to a chart recorder on which the correlation plane cross-sectional scans were obtained.

For the system under test, the detector noise level was measured with no input light incident on the detector. It thus corresponds to the detector dark current and defines the lowest output intensity that the experimental system can detect. The source of this noise is the PMT used to detect and amplify the detected light signals. The scatter level of the system corresponds to the minimum output light level that the optical system can support. This noise level is due to scatter from the many lenses, mirrors and film interfaces present in the system. This measurement was obtained with the MSF in place (to block dc and low spatial frequency data) and with a film of uniform transmittance equal to the average transmittance of the input image in place at the input plane P_1. This scatter level should be above the detector noise level. This requires a light source of adequate intensity and a detector of adequate sensitivity.

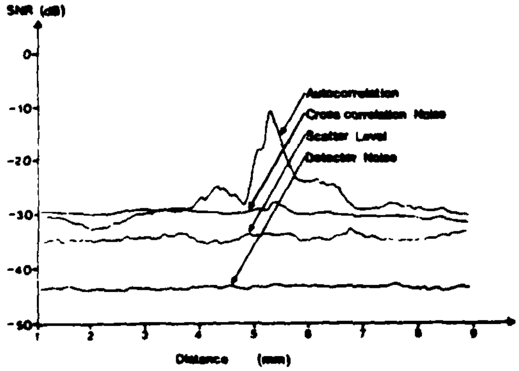

FIGURE 2. Laboratory data showing three types of correlation plane noise.

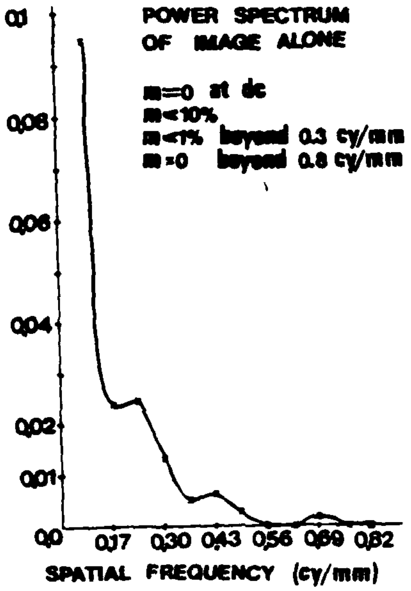

FIGURE 3. Cross-sectional scan of the Fourier transform of a synthetic reference image showing its low modulation and low frequency content.

The correlation pattern contains peak sidelobes and other structural patterns far from the peak. These latter data are part of the actual true correlation and we refer to them as correlation noise. To insure proper measure of the correlation plane SNR, we must insure that the correlation noise level is above the lower of the system's scatter level and the detector noise. If the source's light level, the input data modulation, the diffraction efficiency of the MSF or the detector's sensitivity is too low, the correlation noise will be too low and the measured correlation plane SNR will not be a valid measure of the true SNR of the output data.

For the data in Figure 2, the light levels, η, etc. for the optical system measured are adequate (i.e., the correlation noise level is above the scatter level and the detector

Comment 3

310-25

noise). Lower detector noise levels of 80dB have been obtained with other detectors that we have (i.e., cooled PMT systems, operated in a photon counting mode) Optical systems with better components have been assembled by us and have produced better than 55dB scatter levels. Thus, the data in Figure 2 should be viewed only qualitatively, with attention to demonstrating the three noise sources rather than with attention to the specific noise values listed.

4. DATA MODULATION, BIAS AND SPATIAL FREQUENCY EFFECTS

From our remarks advanced in Section 3 with attention to the three noise terms in Figure 2, the importance of high modulation data should be apparent. In Section 2, we noted that the synthetic reference imagery was of low modulation and spatial frequency. We now quantify these issues. To do this, the Fourier transform of a reference image was optically formed and scanned with a photometric microscope. The Fourier transform of the Rect function aperture was also obtained optically and scanned with the same detector system. Subtracting these two patterns, we obtain an approximate version of the intensity modulation versus spatial frequency in the Fourier transform of the synthetic reference image alone (Figure 3). This plot shows the key quantitative features of the synthetic reference imagery. We first note that the image has no useful spatial frequency data beyond 0.8cy/mm, that beyond 0.3cy/mm the modulation is below 1% and at no spatial frequency is the modulation above 10%. We thus see from this representative data that quite severe light losses will result when correlations are attempted on such synthetic reference imagery. We return to this issue in Section 7.

Another issue associated with this synthetic reference data is how to set $K = 1$ at spatial frequencies below 0.3cy/mm, where more data modulation exists. Since the diameter of the first ring of the wedge ring detector used to set the K beam balance ratio [2] corresponds to a spatial frequency of 0.38cy/mm, setting $K = 1$ in this band is difficult. This issue was further complicated because scatter from the dc and low spatial frequency data precludes accurate setting of $K = 1$ at such low spatial frequencies so close to dc. To facilitate accurate test data on this imagery, we photoreduced it by 4.4X to increase its spatial frequency content and we rerecorded the data on high contrast film. The results of tests on these enhanced imagery are presented in Section 7.

To provide initial quantification of the effects of the bias level b and the modulation level m of the input imagery f(x) plus the effect of the input aperture (assumed for now to be a square of width A), we describe the full input as

$$t(x) = [b + mf(x)]\,\mathrm{Rect}(x/A). \tag{1}$$

One-dimensional functions are used for simplicity with no loss of generality. We can assume that the bandpass filtering action of the MSF removes the bias level and thus set $b = 0$ in (1). A similar zero-mean filtering action can easily be provided in the digital processing of the data. The output correlation then becomes

$$\begin{aligned} c(\tau) &= m^2\, f(x)\mathrm{Rect}(x/A) \circledast f(x)\mathrm{Rect}(x/A) \\ &= m^2 \int_{-A/2}^{A/2-\tau} f(x)f(x+\tau)\,dx, \end{aligned} \tag{2}$$

for $\tau \geq 0$. From (2), we see that a low image modulation m will greatly reduce the amplitude of the correlation output (as is well-known). We also note that the input aperture A will affect the variance of our estimate of the correlation output at shifts $\tau \gg 0$. This occurs because less overlapping image area will be used in (2) for $\tau \gg 0$. We properly normalized the output correlation by using

$$c(\tau) = \frac{m^2}{A-|\tau|} \int_{-A/2}^{A/2-\tau} f(x)f(x+\tau)dx \tag{3}$$

for $\tau \geq 0$. This corrects the optical correlation for the triangular output weighting that would normally result if the images being correlated were not periodically repeated (as occurs in a digital circular correlation). However, the variance of the correlation noise estimate will still be worse as the τ shift is increased as noted in conjunction with (2).

If the bias level b were not completely removed, the correlation obtained would be

$$c(\tau) = Ab^2\Lambda(x/A) + (Am^2/2)(f \circledast f)\Lambda(x/A), \tag{4}$$

where the triangular function $\Lambda(x) = 1 - x$ for $|x| \leq 1$ and is 0 elsewhere. From (4), we see that the contribution to the correlation due to the aperture (first-term) is of amplitude

310-25

Ab^2, whereas the contribution due to the image itself is $Am^2/2$. Assuming $b = 0.5$ and $m = 0.1$, the contribution to the correlation due to the aperture is $2b^2/m^2 = 2(0.5)^2/(0.1)^2 = 50$ times more intense than the image correlation. Suppression of the dc level of the image is thus quite important in MSF pattern recognition.

Our optical correlation experiments have shown that the bias level b is not completely removed by the high pass filtering action of the MSF. Thus, the actual optical correlation output is neither (2) nor (4). Rather, it is similar to (4), but with a lower bias level b than the one present in the original imagery of (1). Moreso, the t(x) input is high pass filtered or differentiated and thus the factor of 50 difference in the aperture and image correlations noted above will be greatly reduced in practice. However, the aperture correlation effect cannot be neglected if m is low as we show in Section 5. An exact analysis of this issue is quite image dependent and appears to be due to the fact that a local digital edge-enhancement operator removes the mean (or bias b) of each part of the image. Conversely, the optical high pass filtering operator (being a global rather than a local operator) removes the average bias level for the entire image and thus does not completely remove the bias level for each part or object in the image.

In conclusion, we note that the width of the aperture correlation term will not be 2A as is implied by (4), but rather will be much narrower with the width approximately given by twice the reciprocal of the bandwidth of the data. This is important, since the image correlation is thus not masked within the wide aperture correlation function. Rather, it is quite well separated (see Figure 4a and Section 5).

5. APERTURE CORRELATION EFFECTS

From Section 4, we have shown the contribution due to the optical output correlation can be significant when the image modulation is low (as it is in Figure 3). We also note that the global versus the local high pass filtering operation of the weighted optical MSF does *not remove* the bias level of each object in the image and thus leaves a potentially large contribution due to the aperture correlation. We now consider techniques to reduce these effects.

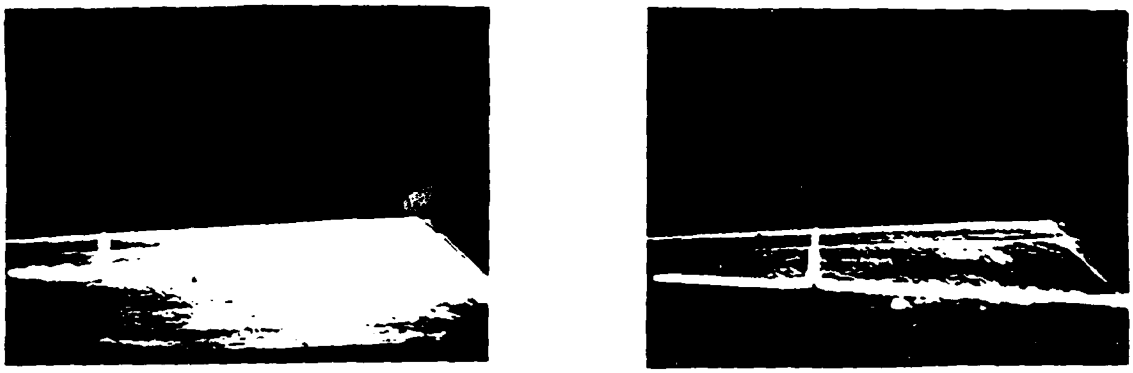

(4a) APERTURE AND IMAGE CORRELATION

(4b) IMAGE ONLY CORRELATION

FIGURE 4. Output correlation plane pattern showing (a) both the aperture and image correlations and (b) only the image correlation (obtained after high pass filtering and use of different apertures for the input and reference imagery).

We describe the reference image to be used as

$$r(x) = [b + mf(x)]\,\mathrm{Circ}(x) \tag{5a}$$

and the input image as

$$t(x) = [b + mf(x + x_0)]\,\mathrm{Rect}(x), \tag{5b}$$

where the input is assumed to be shifted by x_0 from the reference location and where different aperture functions are used for the input and reference images. It is possible to place both the input and reference functions in rectangular apertures of different widths A_1 and

Casasent 5

A_2 or to use different aperture functions directly. In our present description, we assume circular and rectangular apertures for the reference and input imagery, since this was the actual procedure used in the laboratory. As noted earlier, high pass filtered versions $r'(x)$ and $t'(x)$ will be correlated in the actual optical MSF system. The correlation $r' \circledast t'$ will thus contain four terms. Two are the average of f over the aperture regions. With zero-mean imagery, these terms are negligible. The remaining terms are the aperture correlation (located at a fixed position $\tau = 0$) and the correlation of the high-pass-filtered image f' (located at $\tau = \tau_0 = x_0$).

To describe the high-pass-filtered data, we approximate [7] the optical high pass filter (HPF) function as a derivative filter with a bandwidth BW equal to that of the signal $f(x)$. The edges in the differentiated data will thus have a small but finite width (1/BW). For the case of the Rect aperture, we write the derivative function as

$$[\mathrm{Rect}(x/A)]' = \mathrm{Rect}[(x - A/2)BW] + \mathrm{Rect}[(x + A/2)BW], \tag{6}$$

or as two pulses of width 1/BW located at $\pm A/2$. The correlation of r' and t' now contains 25 terms. However many can be eliminated and the resultant expression simplified as we now discuss. We write the terms containing $f(x)$ times the derivative of the aperture function as

$$f(x)d(\mathrm{Aperture})/dx = kd(\mathrm{Aperture})/dx. \tag{7}$$

This is realistic, since the derivative of the aperture function is a circular or rectangular edge (in 2-D) of width 1/BW as in (6) and the image function $f(x)$ only effects the amplitude of this edge at the locations where the two overlap. We represent this factor by the constant k term in (7). The correlation output terms can thus be grouped as

$$\begin{aligned} C(\tau) = {} & [b^2 + 2bkm + k^2m^2][\mathrm{Rect}'(x) \circledast \mathrm{Circ}'(x)] \\ & + [bm + km^2][\mathrm{Rect}(x)f'(x) \circledast \mathrm{Circ}'(x)] \\ & + [bm + km^2][\mathrm{Rect}'(x) \circledast \mathrm{Circ}(x)f'(x)] \\ & + m^2[\mathrm{Rect}(x)f'(x) \circledast \mathrm{Circ}(x)f'(x)] \end{aligned} \tag{8}$$

The second and third terms in (8) are negligible because $f'(x)$ is of zero-mean. The first term will also be negligible since the correlation of the derivatives of two different apertures will have very little in common (i.e., for the case of the circular and square aperture of equal diameter and width, their derivatives only overlap at the four areas in the center of each edge of the square aperture). The resultant correlation thus reduces to the fourth term in (8). Assuming approximately equal areas for the two apertures, we thus write the correlation output pattern as (with $m = 1$)

$$C(\tau) = [f'(x) \circledast f'(x)]. \tag{9}$$

In Figure 4a, we show the correlation output pattern in (4) with the same Rect aperture function used for the input and reference imagery. The natural HPF action of the optical MSF is included. This reduces the aperture correlation term in (4), but, as seen, the aperture correlation peak on the left is still quite appreciable compared to the image correlation peak on the right. (The input image was displaced by x_0 to show these two correlation peaks separately). In Figure 4b, we show the correlation output pattern in (8) using different apertures for the input and reference imagery. The output is the single correct image correlation peak as predicted by (9).

6. COMPARISON OF OPTICAL AND DIGITAL MULTISENSOR IMAGE CORRELATIONS

As our first experimental optical correlations, we considered the processing of various pairs of multisensor images of the same scene (Ames) taken in different wavelengths (see columns 1 and 2 of Table 1). In multisensor image pattern recognition, the edges of the objects in the scene are well-known to be most useful, reliable and reproducable image parts on which to base a pattern recognition correlation. Thus, various edge-enhancement preprocessing techniques have been used in multisensor image detection and registration. In [5], we have explored multisensor image detection in depth. Our present concern is to assess the use of different edge-enhancement preprocessing operators for multisensor pattern recognition and to compare the results of optical and digital correlations on multisensor image pairs.

Table 1. Optical and digital multisensor correlations (Ames data base)

REF $\circledast$ INPUT	SENSOR (μm)	CM	DIGITAL (no preproc)	OPTICAL (HPF)	DIGITAL GRAD	HPF
22 $\circledast$ 22	8-12	1	21.2	15	50.3	X
22 $\circledast$ 23	8-12,Vis	0.371	3.3	4	11.6	8.7
22 $\circledast$ 25	8-12,0.8-0.95	0.269	4.5	6	12.5	6.3
10 $\circledast$ 11	1.06,0.8-0.95	0.81	16.9	15	7.0	X

In column four of Table 1, we show the results of a direct digital correlation on selected multisensor image pairs (with no preprocessing). These should be compared to the results in column five using optical weighted MSF correlations (with the $K = 1$ spatial frequency setting with the best correlation output used). As our performance measure, we use SNR (defined as the ratio of the correlation peak to the variance of the correlation far from the peak). We note that the optical correlation results are comparable to those of the digital correlator with better results obtained optically for most correlation pairs and slightly poorer results obtained for only two multisensor correlations. This is due to the fact that the optical correlator always produces a high pass or band pass filtering action, whereas the full image spectrum is used in the digital correlations. The two cases when better SNR resulted from digitally processed data correspond to the case of an autocorrelation and to an image pair for which the correlation measure

$$CM = \frac{\int I_r(x) I_s(x)\, dx}{[\int I_r^2(x)\, dx \int I_s^2(x)\, dx]^{1/2}} \tag{10}$$

was large (0.81). This correlation measure in (10) is the correlation at registration normalized by the energy in the two images. As shown in [5], large values of CM indicate that the image pairs have significant common information and thus that they are unisensor moreso than multisensor data. In such cases, HPF preprocessing will degrade the output correlation as noted in [5]. Thus, both cases in Table 1 for which optical HPF processing proved inferior correspond to unisensor not multisensor data.

To provide further insight into multisensor pattern recognition and our comparison of optical and digital correlations, a |GRAD| preprocessing operator

$$|\mathrm{GRAD}| = \sqrt{(I_{i,j+1} - I_{i,j})^2 + (I_{i+1,j} - I_{i,j})^2} \tag{11}$$

was applied to both images. The subscripts i,j in (11) refer to image pixel numbers. The correlation results are shown in column 6. A digital HPF preprocessing operation with various cutoff frequencies was also applied to two of the multisensor image pairs. The results for the best cutoff frequency are given in column 7. Comparing the digital |GRAD| operator (column 6) with the optical HPF (column 5), we see that the |GRAD| performs better in all cases except the last one. From [5], we know that the |GRAD| operator whitens the image spectrum and equalizes the polarity of the edges in the edge-enhanced image. The improvement for the autocorrelation of 22 $\circledast$ 22 is due to whitening of this uni-sensor case. The loss for the 10 $\circledast$ 11 case is due to the high CM for this pair of images. The two central correlations noted in Table 1 are typical of most of the results we obtained. They verify that for multisensor imagery (low CM), the absolute value operator improves the output correlation SNR over that obtained with an optical or digital HPF (column 5 and column 7). Comparing columns 5 and 7, we see that the digital HPF gives a better SNR. This is due to the fact that a much lower cutoff frequency (0.23cy/mm) was possible with a digital HPF compared to the optical HPF (0.86cy/mm) due to dc scatter and low image modulation.

Despite these differences, it appears that an optical weighted MSF is adequate for most multisensor pattern recognition (with low $CM < 0.5$ values) if K can be set equal to unity at a low enough spatial frequency band (see Section 7). In Figure 5, we show two of the multisensor images (22 and 25) and the resultant real-time optical output correlation.

Casasent 7

310-25

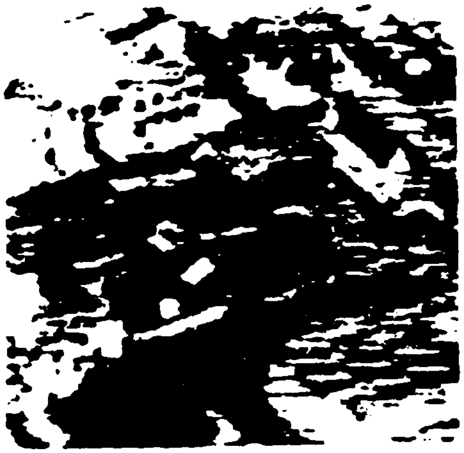
(5a) λ = 8-12μm

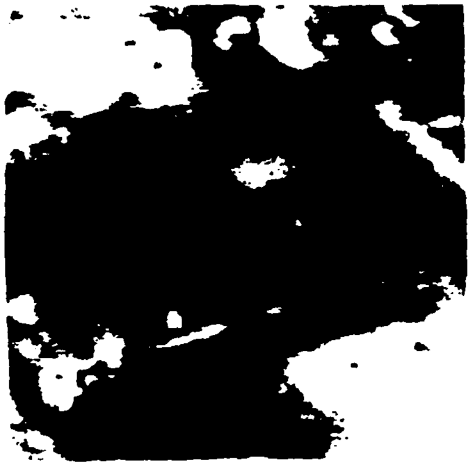
(5b) λ = 0.8-0.95μm

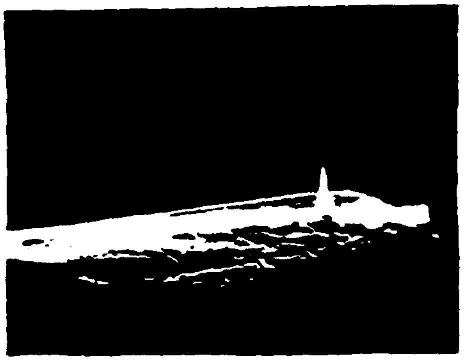
(5c) Correlation

FIGURE 5. Input multisensor imagery (a) and (b) and optical output correlation plane pattern (c).

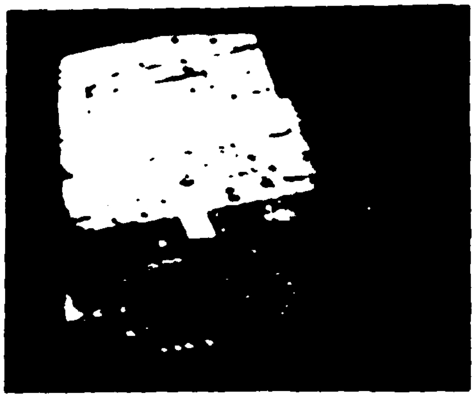
(6a) Sensed (λ = 8-12μm)

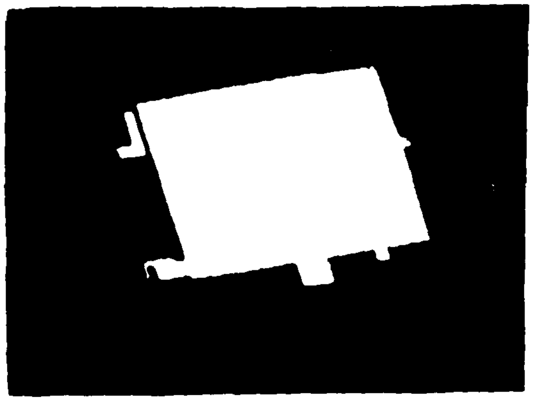
(6b) Synthetic Reference

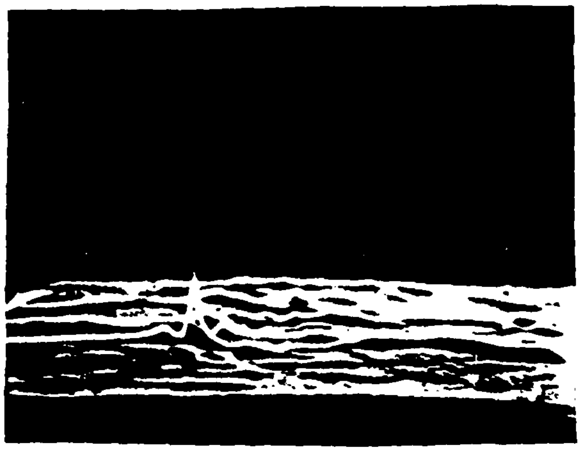
(6c) Correlation

FIGURE 6. Correlation (c) of sensed (a) and synthetic (b) image data after gray tone modification (GTM) preprocessing.

Casasent 8

3 - 27

7. CORRELATION WITH SYNTHETIC REFERENCE FUNCTIONS

As noted in Section 4 and as shown in Figure 3, the modulation and spatial frequency content of the synthetic reference imagery was quite low. To allow optical correlations on these data with measureable SNR_0 values (with the correlation noise level above the system's scatter level, see Figure 2) and with the beam balance ratio set equal to one at a sufficiently low spatial frequency (see Figure 3 and Table 1), it was necessary to photoreduce the data and to apply more sophisticated preprocessing operators. In Figure 6, we show typical reference and sensed input images (Lockheed building). Differences in the contrast, detail on the roof and in image noise (e.g. trees and cars are present in the sensed image, but are absent in the synthetic reference image) are obvious.

We first photoreduced the sensed and reference images in this data set by a factor of 4.4. This effectively increased all spatial frequencies in the data by a factor of 4.4. (Recall from Section 6 and Table 1 that the optimal spatial frequency cutoff found from the digital correlations on the multisensor data was 0.23cy/mm, whereas our optical system could not be used below 0.86cy/mm. Also note from Figure 3 that the synthetic reference imagery has negligible modulation beyond 0.8cy/mm). The photoreduction performed thus allows K to be set equal to one in the more appropriate lower spatial frequency bands. With this step, we expect experimental results that agree with theory.

As new preprocessing operators, we use gray-tone modification (GTM) and small-surface lysing (SSL). These digital preprocessing operations [8] were performed by Technology Services Corporation, who provided us with 35mm transparencies of the sensed and synthetic target imagery with and without these preprocessing operators applied. The GTM operation calculates the number of pixels in the sensed and reference images with given gray level values. It uses this histogram to equate gray levels in the two images with approximately equal distributions. It also performs histogram equalization [9] to allot the optimal portion of the gray level range available to those image regions with appropriately large distributions for a given gray level. Latching is used to provide a good mapping or histogram of the gray levels in the imagery. This preprocessing operator thus makes the gray levels of corresponding regions of the sensed (input) and reference (synthetic) imagery equal plus increases the contrast and modulation of the imagery. From our discussions in Sections 3, 4 and 5, these are both desirable image attributes for optical correlation. The SSL preprocessing operator is used to remove small surfaces that are not connected to larger ones. This is most useful in removing the noise produced by edge enhancement. This operation is achieved by a smart median replacement of all image pixel levels. This is achieved by first determining thresholds for the normalized magnitude of an edge and the correlation length of the image texture from a training set.

Our experimental data obtained on the down-looking ATH data base for the Lockheed imagery are summarized in Table 2. In columns 1 and 2 , we provide the results of correlations with a synthetic reference function with a high u' spatial frequency band setting. In columns 3 and 4, we provide analogous data for the GTM preprocessed synthetic reference with a much lower u' spatial frequency cutoff band emphasized. The different entries in each column correspond to different preprocessed inputs (SYN = synthetic, SEN = sensed, GTM/SSL refers to data with both the GTM and the SSL operators applied). The output correlation plane SNR values for each case are denoted in columns 2 and 4 for comparison.

In these optical correlation experiments, the use of photoreduced imagery allowed lower u' settings to be used and hence more reliable results to be obtained. This was possible because the effects of scatter from dc spatial frequency data was decreased with the increased image spatial frequency provided by the photoreduction. All SNR values with the GTM preprocessed synthetic reference (column 4) exceed those obtained with the original unpreprocessed synthetic reference (column 2). As row 1 in Table 2 shows, the GTM operator improves the SNR of the autocorrelation (due to the increased data modulation provided). As row 2 shows, better cross-correlations were obtained with the GTM preprocessed reference and even better results (column 4) with a GTM preprocessed sensed image also. The SSL operator alone (row 5) gave poor results and when used in conjunction with the GTM operator (row 4), the results obtained were inferior to those of the GTM operator alone. These data lend credence to further studies of these and other more advanced preprocessing operators. The decrease in performance obtained when the SSL operator was used (even if used in conjunction with the GTM operator) indicate that more analysis and attention should be given to the details of this operation (i.e. any image distortion it introduces, any image modulation decrease it produces, and any true image data it removes). Additional experiments performed with the SSL operator on data with a large number of independent objects indicates that the latter issue may be of major concern in future work. In Figure 6c, we show the optical correlation output obtained from the given sensed and synthetic reference functions shown in Figures 6a and 6b.

Comment 9

310-25

Table 2. Correlations with synthetic reference imagery using various preprocessing operators (Lockheed database).

SYNTHETIC REF		GTM (SYN) REF	
u' = 1.05-1.8 cy/mm		u' = 0.22-0.41 cy/mm	
INPUT	SNR (dB)	INPUT	SNR (dB)
SYN	16	GTM (SYN)	19
SENSED	6.5	SENSED	8
GTM (SEN)	5.5	GTM (SEN)	10
GTM/SSL (SEN)	4.0	GTM/SSL (SEN)	9.5
SSL (SEN)	2.0	SSL (SEN)	3

8. SUMMARY AND CONCLUSION

In this paper, various aspects of image quality and its effects on the output correlation from an optical weighted matched spatial filter correlator were addressed. The fixed pixel pattern of the input using digitized data was noted and the effect removed by the use of a simple spatial frequency in the transform plane. Three sources of optical correlation plane noise were then noted and the effective data modulation, spatial frequency and input aperture effects were discussed for each. Low spatial frequency data often precludes setting K at sufficiently low spatial frequencies. Use of photoreduced imagery was shown to overcome this problem. Synthetic reference imagery was found to have low modulation and very low spatial frequency data. The correlation of this reference data was found to be possible with the use of advanced digital preprocessing operators such as gray-tone modification and small surface lysing. Aperture correlations were found to dominate all image correlations. This effect was overcome by the use of different apertures for the input and reference function together with high pass filtering. A comparison of optical and digital correlations on multisensor imagery showed that the high pass filtering action performed by the weighted matched spatial filter correlator was appropriate for the majority of multisensor image pattern recognition problems (this class of multisensor imagery was found to be measureable by a correlation measure, the energy normalized correlation at registration). From these studies, much new insight on the effect of image quality on the performance of an optical matched spatial filter correlator have been determined together with the use of weighted matched spatial filter high pass filtering for multisensor pattern recognition and the need for advanced preprocessing techniques in correlations with synthetic reference imagery.

ACKNOWLEDGEMENTS

The authors thank the Analytical Sciences Corporation and Grumman Aerospace for supplying us with some of the imagery used in these experiments. We also thank Technology Services Corporation for providing us with the GTM and SSL preprocessed imagery used. We also gratefully acknowledge the support of the Air Force Office of Scientific Research (Grant AFOSR 79-0091) for continuing support of our optical data processing for missile guidance research program.

REFERENCES

1. A. Van Der Lugt, IEEE, IT-10 (1964).

2. D. Casasent and A. Furman, Applied Optics, 16, 1652, 1662 (1977).

3. D. Casasent, Proc IEEE, 67, 813 (1979).

4. B. Chang and C. Leonard, Applied Optics, 18, 2407 (1979).

5. Y. Barniv and D. Casasent, SPIE, 292 (1981).

6. B. Berkeley, MS Thesis, CMU (April 1980).

7. B. Kumar and D. Casasent, Optics Communication, (January 1980).

8. R. Keller et al, Proc Pattern Recognition Conference, 937-942 (December 1980), IEEE Catalog No. 80CH1499-3.

9. R. Gonzalez and P. Wintz, Digital Image Processing, Addison-Wesley, 119-127 (1977).

SECTION 5

MULTI-SENSOR PATTERN RECOGNITION

(EXPERIMENTAL VERIFICATION OF THEORY)

232-13

MULTISENSOR IMAGE REGISTRATION: EXPERIMENTAL VERIFICATION

Yair Barniv* and David Casasent

Carnegie-Mellon University, Department of Electrical Engineering
Pittsburgh, Pennsylvania 15213

*Present Address: Systems Control, Inc., 1801 Page Mill Road, Palo Alto, California 94304

ABSTRACT

A general multisensor image processor and image model are described and experimental verification of their use are provided. The pixel correlation coefficient is shown to be an adequate measure of the statistical independence of the gray levels in a multisensor image pair and to be of use as a guide to selecting various preprocessing operators. Experimental results obtained on the various multisensor image data bases verify our theory quite well and have contributed considerable practical insight into the processing of imagery with random contrast reversal intensity differences.

1. INTRODUCTION

In nearly all practical pattern recognition and image registration applications, the input and reference images can differ in a variety of ways and for many diverse reasons. In this paper, we consider the registration or recognition of images of the same scene when the images originate from different sensors or from the same sensor under different conditions. The latter case arises in infrared imagery and can also be due to differences in weather, seasons, sun angle, time of day, etc. We term all such data as multisensor imagery (MSI). We distinguish MSI from unisensor imagery (USI) data by noting that in MSI data, the gray level of the same object in different images is independent. When total independence exists, we refer to the data as pure MSI. When total dependence occurs, we classify the data as USI.

Much MS imagery lies between the extremes of pure MSI and pure USI data. As our measure of the class of imagery, we use the pixel correlation coefficient for a reference I_r and sensed I_s image pair,

$$\rho = \frac{\int I_r(x) I_s(x)\,dx}{[\int I_r^2(x)\,dx \int I_s^2(x)\,dx]^{1/2}} . \tag{1}$$

~~One-dimensional~~ functions are used for simplicity and the correlation peak is asssumed to occur at the origin with no loss in generality. The ratio in (1) of the intensity of the correlation at registration to the product of the energies in the two images is thus a useful normalized measure of how well they correlate. When $\rho = 1$, the imagery is pure USI. Whereas, when $\rho = 0$, the data is pure MSI.

As our performance measure, we select the output signal-to-noise ratio SNR_0 in the correlation plane, defined by

$$SNR_0 = \frac{E\{c(0)\}}{\sqrt{Var\{c(\tau)\}}\big|_{\tau>>0}} . \tag{2}$$

The numerator in (2) is the expected value of the correlation at registration $\tau \equiv 0$ (with the expectation taken over all scenes and conditions). The denominator is the standard deviation of the output correlation far from the correct registration point. This SNR is easily measured in the laboratory and it can be related to other SNR measures as well as to the probability of detection P_D, the probability of false alarm P_{FA}, the probability of correct registration P_C and the probability of error P_E. It is thus a most appropriate parameter to use in comparing various image registration systems.

A wealth of work in MSI registration exists. However, in some cases (e.g. [14]), the data used does not exhibit random contrast reversals. Moreso, no noise was present in several of the cases analyzed (e.g. [15]). Thus, such cases actually typify USI data rather than MSI data. Moreso, no particular preprocessing operations or techniques are necessary to register such imagery. In our work, we are concerned with pure MSI data, with those image features that give rise to such data, and with the optimal processor to be used for such data recognition problems. Many heuristic methods have been advanced and used to register MS data. These involve optical [1,2] and digital[3-5] systems, and edge detection techniques [6,7] and template-matching methods [8,9]. The most successful results have been obtained using gradient edge detection preprocessing operators followed by correlators [3,10-12].

Casasent

292-13

Our work makes use of this prior art. However, we envision a hybrid optical-digital processor in which the preprocessing operations are performed digitally and the correlation is performed optically. We also adopt a more fundamental and basic approach to this MS registration problem that includes a supporting image model and a general MSI processor architecture. This model and general processor [13] are summarized in Section 2. The highlights of our statistical analysis of this processor were provided earlier [13]. In this paper, we thus concentrate on the experimental verification of these results. In Section 3, we first show that conventional correlation cannot work for MSI data and we advance a communication analogy for this problem. Our results provide considerable insight into the nature of the MSI registration problem. Following a description of the MSI data bases used (Section 4), experimental data on six aspects of MSI registration are advanced. These include: the use of ρ as a measure of the type of imagery (Section 5), how the number of objects in the image affects the result (Section 6), the need for Gaussian-histogram reshaping (Section 7), verification of our MSI model (Section 8), a comparison of high pass filtering, gradient and image whitening operators (Section 9) and threshold selection when noise is present in the data (Section 10).

2. IMAGE MODEL AND MULTISENSOR PROCESSING ARCHITECTURE [13]

We define an object as a region with a homogeneous gray level, separated from other objects by edges. Although the gray levels of the same object in different MSI are statistically independent random variables, the edges of the objects are preserved in the MS imaging process. In our mathematical model of pure MSI data, the scenes to be registered are assumed to contain objects larger in extent than several pixels. We assume zero-mean data. This is directly realized in optical matched spatial filter processors. In digital processing, this assumption is equivalent to removing the mean of the data. Since the mean of the data does not provide reliable information, such an assumption is practical and necessary.

A cross-sectional scan through a MS image is thus assumed to yield a train of pulses whose amplitudes and locations are random variables. The location of the pulses (image edges) are assumed to have a distribution that corresponds to a low-density Poisson statistical distribution with an average pulse rate λ per unit distance. The amplitudes of the pulses are assumed to have zero-mean Gaussian density functions. We assume white zero-mean Gaussian noise to be added to the sensed image. We also assume the pulse trains, their amplitudes and noise to be stationary and statistically independent.

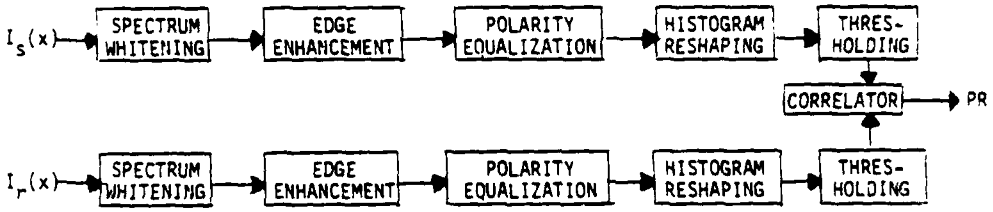

FIGURE 1 General MSI Pattern Recognition Processor

Our general MS processor model considers five preprocessing operators (applied to both the reference I_r and the sensed I_s images) followed by a correlator as shown in Figure 1. Spectrum whitening refers to producing data spectra that are white (i.e. with the Fourier transforms of the image plus noise being uniform for both the sensed and reference imagery). Since the edges of the objects are the common features that are preserved in MS image pairs, edge-enhancement is a necessary preprocessing function for MSI registration. However, since the gray levels of all objects in an image are random, then so are the polarities of all of the edges in an edge-enhanced image. We thus also consider a simple nonlinear absolute operator and its use in equalizing the polarity of the edges in an edge-enhanced image pair. We will consider various edge-enhancement operators separately. However, experiments have shown (Section 3) that edge-enhancement operators generally also provide approximate whitening operations. Thus, in practice, both of these preprocessing operators are included as one rather than separately. We find the gradient operator to work quite well and thus we compare the need for polarity equalization by applying the signed gradient operator (SGN) and the absolute value |GRAD| gradient operator to the same image pair and comparing the resultant output correlation SNR_0. We use the approximate |GRAD| operator

$$|\mathrm{GRAD}|_{i,j} = \sqrt{(I_{i+1,j} - I_{i,j})^2 + (I_{i,j+1} - I_{i,j})^2}, \tag{3}$$

for the absolute value of the gradient at pixel (i,j) of image I because it is easily realized digitally and because experimental verification indicates that this operator is quite useful.

A histogram reshaper is the next preprocessing operator we consider. To use a correlator as the final image registration step, the histogram of the pixel's gray levels in the imagery should theoretically be Gaussian. Forming the magnitude of the gradient of an image is a quite nonlinear operation that is expected to significantly change the pixel's histogram. We consider the importance of the pixel's histogram distribution by applying the nonlinear mapping

$$Y = \log(X + 1) \tag{4}$$

to the histogram of the ordered pixel gray levels X. This histogram reshaping function was found empirically to approximately produce the Gaussian histogram theoretically needed for a correlation image registration processor. The threshold operator is applied to the pixel intensity levels X to reduce additive noise in the data prior to correlation. This simply involves replacing pixels with intensity levels $X \leq Th$ and $X > Th$ by new values Y such that

$$Y = \begin{cases} 0 & , X \leq Th \\ X-Th & , X > Th \end{cases} . \tag{5}$$

In Sections 5 - 10, we present the results of various experimental studies of these different preprocessing operators and other issues associated with the image model and general multisensor processor. For example, we consider: the Poisson pulse rate λ, number of objects present in the image, threshold selection, input SNR_i, other edge-enhancement operators, and image-whitening operators. Theoretical analyses of the image model and the MS processor architecture were advanced earlier by us [13]. Thus, our present emphasis is on the experimental verification of the predicted results.

3. USI AND MSI PROCESSING

To provide insight into the differences between USI and MSI data and the processing necessary to register each, we highlight the results of a statistical analysis of conventional correlation (with no preprocessing) applied to pure MSI data. We also advance a communications analogy by which the potential need for the various preprocessing operators included in our MS processor model of Figure 1 can be seen. For computational reasons, we use the correlation SNR, defined as the ratio of $c(0)$ to the standard deviation of $c(\tau)$ for $\tau >> 0$ as our performance measure. Applying standard statistical assumptions about the data, it is quite easy to show that both $c(0)$ and $c(\infty)$ are zero-mean Gaussian random variables with standard deviations of $\sigma_0/\sqrt{n}$ and $\sigma_0/\sqrt{kn}$ respectively. In this notation, σ_0 is the standard deviation of an object of area equal to that of the full image, n is the number of independent objects in a given image and kn (where $k > 1$) is the number of apparent objects present in the overlap of two MS images far ($x = \infty$) from registration. In practice, $\sigma_0/\sqrt{kn}$ is a lower bound on the correct standard deviation.

Replacing the standard deviation by its average, or the statistical variance, the SNR_0 is seen to be a zero-mean Gaussian random variable with standard deviation $\sqrt{k}$. Thus, for any desired $SNR_0 = Th$, P_D is non-zero and P_D increases as k increases (and hence as the number n of independent objects in the image increases). For $k = 4$, we find $P_D < 10^{-6}$ for even a low desired SNR_0 of 10. The problem of correct registration P_C was also derived for this case. We found that for $n = 50$ and $k = 3.2$, P_C was $\approx 10^{-2}$. Moreso, we showed that a random choice of any correlation peak, rather than selection of the largest one, gave a better P_C value. Thus, conventional correlation on MSI data is seen to yield quite poor performance.

Whitening the spectrum of imagery improves the performance of USI correlations, but is of no use in MSI correlation because it simply increases the amplitude of all peaks in the correlation plane (the correct peak as well as all sidelobes). It also increases n and thus decreases P_C for MSI data even more. For USI data, the overlap of two images have positive random variables with a positive mean probability density function (rather than a zero-mean probability density function as occurs in MSI data). Thus, for USI data, SNR_0 is proportional to $\sqrt{n}$ and P_C improves as n increases, whereas for MSI data SNR_0 is independent of n and P_C degrades as n increases (unless other preprocessing operators are used). Thus, increasing n by whitening improves the performance of a USI correlator, but degrades the performance of an MSI correlator. This insight is useful in explaining why various preprocessing operators appear to be useful in some MSI registration applications, but not in others. In some MSI registration work, the image was dominated by one key object, in which case $n = 1$. For this case, the conventional correlation applied to such data will yield satisfactory results (simply because the data is really USI not MSI).

In our work, we are quite concerned with the fact that the results of the ad hoc applica-

Casasent

tion of different preprocessing operators to image pairs (with no attention to the image models) not be extended to the general case. We summarize these remarks in Table 1 and re-emphasize the difference between USI and MSI data. Our ρ measure in (1) is useful in this regard. For pure USI data, $\rho = 1$; whereas for pure MSI data, $\rho = 0$. When $n >> 1$, $\rho \approx 0$ and conventional correlation is useless. When SNR_0 approaches zero, so does ρ. However, if ρ is large (≈ 1), SNR_0 can still be low (e.g. if the image is a periodic function). Note that ρ need only be evaluated at one point (the correct registration point). Thus, we can calculate ρ for a few representative image pairs in a large image ensemble and use the preprocessing appropriate for that ρ value for the entire image data set.

Table 1. Dependence of USI and MSI statistics on n (Whitening only)

	PDF of Correct Peak		PDF of Sidelobe		SNR	P_c
	Average	Standard Deviation	Average	Standard Deviation		
USI	$\propto\sqrt{n}$	$\propto\sqrt{n}$	0	$\propto\sqrt{n}$	$\propto\sqrt{n}$	Increases as n increases
MSI	0	$\propto\sqrt{n}$	0	$\propto\sqrt{n}$	INDEP	Decreases as n increases

In image registration, the correlation length η of the data is another parameter useful in analysis (especially concerning spectrum whitening). If $\eta \approx 0$, an image (or more properly speaking, its pixels) is (are) said to be uncorrelated and its spectrum is nearly white. In the more common case, $\eta \neq 0$ and often $\eta \approx 1$ and then the image (or its pixels) is (are) highly correlated. Much work on image enhancement and spectrum whitening exists [4-5, 15-17]. However, quite different cases (no noise and noise), performance measures and applications were considered in these works. A summary of this work is thus of use in clarifying the results obtained and the different cases being addressed. In missile guidance, we first distinguish between the acquisition phase of image registration (in which the problem is to detect the image) and the homing phase (in which the accurate registration or location of the sensed image within the reference image is of concern). Our SNR_0 in (2) is appropriate for the first case; whereas in the second case our concern is to minimize the variance of the correlation at the peak location (in this case, the denominator in (2) is replaced by the variance of the correlation at the registration peak point). In this second case, a correct registration is assumed to have been determined and the concern within the image registration processor is the accurate location of the correct registration point.

Our immediate concern in this present work is to optimize P_D rather than to optimize registration accuracy. However, much of the prior work on both problems is of use. For the case of no noise and when $\eta \approx 0$ (a white image spectrum), optimization of the SNR_0 in (2) requires the use of only a simple conventional correlator [15]. When $\eta \approx 1$, optimization of the SNR_0 in (2) requires the application of a second derivative preprocessing operator to one of the images prior to correlating them. It has also been shown [5] that applying a second derivative operator to one image is equivalent to applying a first derivative operator to both images. Since the work in [15] assumed no noise in the data, it is of minimal concern to us, since simpler techniques such as simple image differencing can be used in such cases rather than correlations. When noise is present in the images and when the correct registration point has already been determined, optimization of the image registration accuracy can be considered. In this case, a noise-whitening filter is necessary [4,17] and a matched spatial filter system results in which both inputs are first whitened with respect to the noise. Using conventional noise models, the noise-whitening is shown to be equivalent to a first derivative plus a mixed derivative operator. Thus, for the USI case, both approaches are comparable and result in the need for a derivative preprocessing step. In the noise case, this image differentiation performs the necessary spectrum whitening with respect to the noise.

Although no formal analysis of the case of detection optimization on MSI data with noise present has been advanced, we can use this prior work [15-17] and a communication analogy to develop the optimum processor for our MSI case. In this case, we model the additive noise $\hat{n}$ as the sum of the input noise plus the sensed image evaluated far from the correct registration point. We find that the reference and sensed images should both be whitened with respect to $\hat{n}$ prior to correlation. A more important observation that results is that optimization of the SNR at the correlation peak (for registration accuracy optimization) is not equivalent to optimization of our detection SNR in (2) unless the noise spectrum has statistics similar to the imagery itself. In the cases for which this technique has been used [4, 16,17], this has been the case, since the noise in the imagery was defined as the difference between the images. In this case, the statistics of the noise $\hat{n}$ in the imagery happens to agree with our $\hat{n}$ definition by implicit assumption and thus the techniques in [4,16,17] are appropriate. However, for general MSI data, the noise and image statistics differ and our techniques are necessary (i.e. whitening both the reference and sensed images with respect to $\hat{n}$ and applying Gaussian histogram reshaping).

Comment 4

A subtle point associated with our communication analogy is that we do not assume the a priori use of a correlator. Rather, we derive it and include the Gaussian histogram reshaping outcome of that derivation in our architecture of Figure 1. From these considerations and by proper analysis of prior work, our general MS registration system of Figure 1 resulted. From our assumptions on the low frequency of image edges in our model, practical imagery is expected to have low n and thus the first derivative operator is expected to approximate an image whitening operator. We thus include these considerations and our observation that the polarity of the edges in a differentiated image should be equalized by a nonlinear operator such as the absolute value operator (for MSI data) and we thus consider the use of the |GRAD| operator in (3) to perform the three operations of spectrum shaping, edge-enhancement and polarity equalization shown in Figure 1.

4. MSI DATA BASES

To experimentally verify the theory, remarks and models advanced in [13] and in Sections 2 and 3, six real and synthetic MS image data bases were used. Two sets of color images of the same scene in the blue, green and red primary color bands were used as simulated MS data. Our results indicated that such data were nearly pure USI. Any preprocessing was found to yield poorer results than a conventional correlation (as predicted from Section 3). Any threshold operator (with any choice of the threshold) also gave poorer results (due to the high SNR_i of the data) since this operator actually removed low intensity image data rather than noise. This is also in agreement with the theory in [13] which indicated that for large SNR_i data, the optimum threshold was zero. Thus, no experimental results are included on this data, although the results obtained clearly affected our analysis and selection of future MS image data bases.

We used real downlooking planimetric imagery of Ames Research Center (MS data base 3) taken in three MS bands (Table 2) to analyze the effects of ρ and SNR_i on the need for the |GRAD| = GRD preprocessing operator. Our results are presented in Section 5. We refer to this data base as downlooking target (DLT) imagery. In Tables 3 and 4, we summarize the contents of our MS image data bases 4 and 5. We refer to these as short range targetlooking (STL) and long range targetlooking (LTL) respectively. They contain images of the same Ames site as in Table 2 but at a depression angle of 30° and with a slant range of 2880 feet and an altitude of 1440 feet (STL data of Table 3) and with a longer slant range of 5000 feet and an altitude of 2550 feet (LTL data of Table 4) corresponding to the same 30° depression angle. The major difference in these data are the larger number n of objects present in the LTL data compared to the STL data. In Section 6, we analyze how the number n of objects in the image affects the SNR_0 obtained. The effects of Gaussian histogram reshaping on the correlation of these data are addressed in Section 7 and verification of the MSI model advanced in [13] and summarized in Section 2 is provided in Section 8 for these data.

Table 2. Downlooking target (DLT) Ames data base

IMAGE	SENSOR	$\lambda(\mu m)$
S8	Thermal IR	8-12
S10	Near IR	1.06
S11	Near IR	0.8-0.95

Table 3. Short range (2880 feet) targetlooking (30°) (STL) Ames data base

IMAGE	SENSOR	$\lambda(\mu m)$
S2	Thermal IR	8-12
S3	Visible	0.38-0.73
S4	Near IR	1.06
S5	Near IR	0.8-0.95

Table 4. Long range (5500 feet) targetlooking (30°) (LTL) Ames data base

IMAGE	SENSOR	$\lambda(\mu m)$
S22	Thermal IR	8-12
S23	Visible	0.38-0.73
S24	Near IR	1.06
S25	Near IR	0.8-0.95

A simulated MSI data set (denoted by SMS) was also prepared by generating and randomly adding circles of different radii, central locations and gray levels. The SMS image data pairs so generated represent pure MSI data. In Section 9, we compare the use of high pass filtering (HPF) and the |GRAD| operators to the whitening (WIT) operator for this synthetic data as well as for the LTL data set. Our primary use of the SMS data is in verification of the optimal threshold level to use (see Figure 1 and [13]) as a function of the edge pulse rate λ and the SNR_i of the input data. In Section 10, we analyze this issue by adding controlled amounts of white Gaussian noise to the SMS data, performing the indicated preprocessing and comparing the results for various threshold and SNR_i levels. Our summary and conclusions are then advanced in Section 11.

As indicated in Tables 2-4, we denote the different image pairs used in all digital correlation simulations by specific numbers S2 - S25. The simulated imagery are referred to as SIM1 - SIM4, where $\lambda = 14$ objects per image length are used for SIM1 and SIM2 data and $\lambda = 10$ for SIM3 and SIM4 data. We denote the preprocessing operator used by the abbreviations: SGN (gradient with sign preserved), GRD (absolute value of the gradient as defined in (3)), GAS (absolute value of the gradient with Gaussian histogram equilization applied) following the image number. We denote the different high pass filtered versions of each image by FIL1, FIL2, etc. and the absolute values of these images by AFIL1, AFIL3, etc. (see Section 9). Our experimental data generally contain experiment number, input image pairs correlated, the output correlation SNR_0 value obtained, the measured ρ value for the image pair and remarks on the experiment as necessary.

5. ρ MEASURE AND |GRAD| OPERATOR

In Table 5, we list our experimental data obtained on the DLT data base of Table 2. Experiment one shows the large $\text{SNR}_0 = 21.3$ autocorrelation obtained. Comparing correlation patterns from experiments one and two (Figure 2) shows that the |GRAD| preprocessing operator yields a larger SNR_0 value and a narrower correlation peak width (due to the spectrum whitening produced by the edge-enhancement operator). Comparing the results of the cross-correlation experiments three and four (Figure 3), we see that for a low ($\rho = 0.26$) correlation coefficient value (as occurs here), SNR_0 is remarkably improved by the |GRAD| = GRD preprocessing operator. From Table 5 (see * note) and Figure 3, we also note that the registration accuracy of the correlation on GRD preprocessed data is better. Similar results are obtained (experiments five and six) for image pairs eight and ten (because of their low $\rho = 0.28$ correlation coefficient). However, for image pair ten and eleven (experiments seven and eight), their $\rho = 0.81$ value was quite large. This is due to the common polarity of the edge data in this image pair. This image pair thus corresponds to USI rather than MSI data. The observed 4.8 loss in SNR_0 of the GRD preprocessed imagery for this pair verifies the theory advanced in [13] and Sections 2 and 3. From these experimental data, we conclude that ρ is a good measure of whether a given image pair is USI or MSI (with $\rho = 0.5$ being an approximate break point). We also conclude that GRD preprocessing improves the correlation SNR_0 of MSI imagery and degrades that of USI imagery and that better registration accuracy and narrower correlation peaks result from the use of GRD data and thus that spectrum whitening is performed by the GRD operator. More experimental data than the small sampling given in Table 5 was obtained and used to support our conclusions. However, space permits the inclusion of only selected but representative examples of these results.

6. EFFECT OF THE NUMBER n OF OBJECTS

In Table 6, we summarize the results of correlations obtained on the STL and LTL image data bases with attention to the SNR_0 improvement obtained using the GRD operator as a function of the number of objects n in the input imagery. In experiments one and two, we show the autocorrelation SNR gain (9.8 vs 21.2) obtained due to the larger number of objects n present in the LTL data*. In experiments three-four and five-six, an SNR_0 improvement of 2.3 vs 3.1 and 2.9 vs 6.4 were obtained with the GRD preprocessing operator. This corresponds to an average SNR_0 gain by a factor of 1.8 for the STL data. In experiments seven-eight and nine-ten, we consider similar data for the long range imagery (LTL) containing more objects. The SNR_0 improvements (3.3 vs. 11.6 and 4.6 vs 14.4) represent a much larger gain factor of 3.4. From these data, we conclude that the use of the |GRAD| = GRD preprocessing operator becomes more necessary and improves the performance obtained by a larger factor as the number n of objects in the image increases (and hence as the imagery more closely approaches that of our pure MSI model). As before, additional data beyond that included in Table 6 is available to substantiate these conclusions. In addition, the image registration accuracy is better and the width of the correlation peak is narrower when GRD preprocessed data is used. These trends verify our theoretical remarks advanced in [13] and Section 3.

---

* Larger n also means large Signal Bandwidth Product (SBWP).

Casasent

292-18

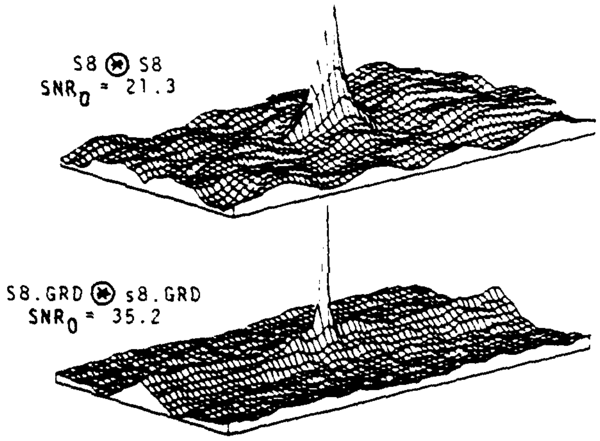

Figure 2 Demonstration of the whitening effect, increased SNR$_0$ and narrower correlation peak width obtained by the GRD = |GRAD| operator.

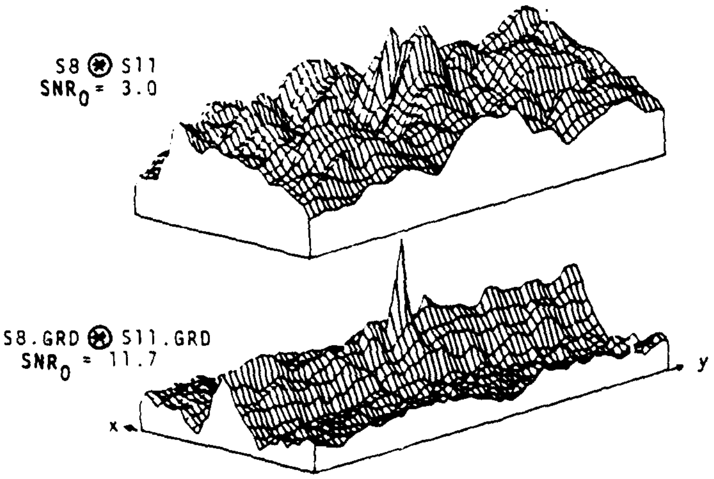

Figure 3 Low ρ = 0.26 data implies poor registration accuracy and low SNR$_0$. |GRAD| = GRD increases SNR$_0$, whitens image spectrum (narrower peak) and gives better registration accuracy.

Table 5. Correlation data for the DLT data base

EXPERIMENT	INPUT-REF	ρ	SNR_0	COMMENTS
1	S8⊗S8	1.0	21.3	Auto correlation
2	S8.GRD⊗S8.GRD	1.0	35.2	Auto (∴USI), GRD does whitening
3*	S8⊗S11	0.26	3.0	ρ is small, thus MSI; GRD improves SNR_0
4	S8.GRD⊗S11.GRD	0.36	11.7	
5*	S8⊗S10	0.28	2.9	ρ is small, thus MSI; GRD improves SNR_0
6	S8.GRD⊗S10.GRD	0.22	7.0	
7	S10⊗S11	0.81	16.9	ρ is large, thus USI; GRD degrades SNR_0
8	S10.GRD⊗S11.GRD	0.48	12.1	

*Peak location in error by 3 pixels

Table 6. Effect of number n of objects on MSI Correlations

EXPERIMENT	INPUT-REF	ρ	SNR_0	COMMENTS
1 STL	S2⊗S2	1.0	9.8	More objects, more SBWP and larger autocorrel SNR_0
2 LTL	S22⊗S22	1.0	21.2	
3 STL	S2⊗S4	0.23	2.3	Average |GRAD| improvement is 1.8
4 STL	S2.GRD⊗S4.GRD	0.08	3.1	
5 STL	S2⊗S5	0.33	2.9	
6 STL	S2.GRD⊗S5.GRD	0.24	6.4	
7 LTL	S22⊗S23	0.37	3.3	Average |GRAD| improvement is 3.4
8 LTL	S22.GRD⊗S23.GRD	0.26	11.6	
9 LTL	S22⊗S25	0.27	4.6	
10 LTL	S22.GRD⊗S25.GRD	0.29	12.5	

7. NEED FOR GAUSSIAN HISTOGRAM RESHAPING

We now consider the LTL image data base with attention to the improvement obtained by use of the GAS preprocessing operator (including Gaussian histogram reshaping) compared to the GRD (magnitude of the gradient) preprocessing operator alone. Comparing the results of experiments one-two in Table 7, we find a gain of 6% for the autocorrelation case. From experiments three-five a 13% gain is observed due to the GAS vs the GRD preprocessing operator. From experiments six-eight, a larger 32% gain is found. From these brief experiments and others, we conclude that the addition of a Gaussian histogram reshaping preprocessing operator can provide a 15% average improvement in SNR_0. Analogous data taken on our SMS imagery agree with these results.

Table 7. Improvement obtained (LTL) by Gaussian Histogram Shapening

EXPERIMENT	INPUT-REF	ρ	SNR_0	COMMENTS
1	S22.GRD⊗S22.GRD	1	50.3	6% Gain
2	S22.GAS⊗S22.GAS	1	52.9	
3	S22⊗S23	0.37	3.3	13% Gain
4	S22.GRD⊗S23.GRD	0.26	11.6	
5	S22.GAS⊗S23.GAS	0.32	13.1	
6	S22⊗S25	0.27	4.6	32% Gain
7	S22.GRD⊗S25.GRD	0.29	12.5	
8	S22.GAS⊗S25.GAS	0.36	16.5	

8. VERIFICATION OF THE MS MODEL

In Figure 4, we show the cross-sectional scans through column 71 of images S22 and S25 after GRD preprocessing. Close scrutiny of the data is necessary to identify common edges in the two scans. To facilitate such an analysis, eighteen of the common edges in these two images have been labeled in Figure 4. From this figure, we note that the amplitude of the common edges differs quite significantly between the two images and that all edges are not ideal delta functions (but rather that their widths depend upon the sharpness of the edge transitions in the original data). From an analysis of these and other cross-sectional image scans, the validity of our MS image model advanced in [13] and summarized in Section 2 has been verified. For our SMS data, nearly exact λ values (low-density Poisson data rates per unit image length) of $\lambda = 10$ and 14 were obtained, measured and experimentally verified (see Sections 9 and 10).

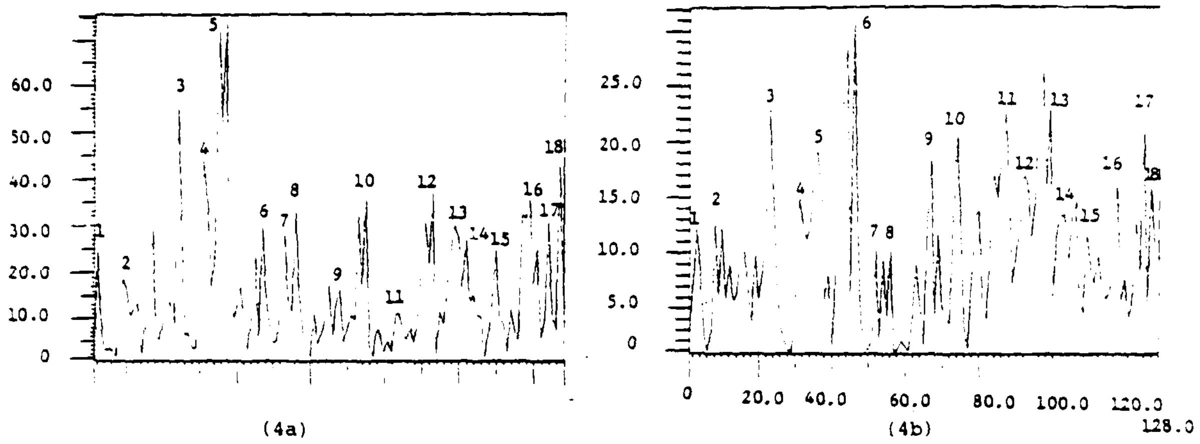

(4a)

(4b)

Figure 4 Cross-sectional scans through column 71 of images S22.GRD (left) and S25.GRD (right) verifying our MSI model.

9. COMPARISON OF HPF, GRD AND WIT OPERATORS

The |GRAD| preprocessing operator appears attractive for edge-enhancement and whitening of MS data, where polarization equalization is necessary. A high pass filter (HPF) is another attractive edge-enhancement operator, since it can be realized optically and is inherently present in the synthesis of a matched spatial filter [18]. It is straightforward to show that the width of the pulses in the train of pulses produced by the HPF version of an image decreases as the cutoff frequency f_0 of the HPF is increased and that the energy in the pulses and hence the useable data modulation also decreases as f_0 increases. Conversely, the area of the pulses produced by the GRD operator is constant. We thus expect the GRD operator to be superior to the HPF edge-enhancement operator.

In Table 8, we summarize the results obtained using the GRD, HPF, and |HPF| operators for the LTL data base. To properly compare these operators, various f_0 HPF cutoff frequencies were tried and only the ones with the best SNR_0 are reported. The HP filters are denoted by the suffix FIL (filter) following the image number. The results of correlations on data preprocessed using the absolute value of the HPF operator are denoted by the suffix AFIL (the best filter cutoff frequency was again used in these experiments). The results in Table 8 are easily explained. First, we note that the HPF preprocessed data (experiments two and seven) yield better SNR_0 than was obtained with no preprocessing (experiments one and six). This indicates that the image pairs are not pure MSI, since if they were, $SNR_0 = 0$ would have been obtained (see Section 3). The absolute value of the HPF operator shows a loss in SNR_0 in both cases. This occurs because the polarity of the edges in the image pairs contain common information (again, this occurs because the data are not pure MSI). The GRD operator yields larger SNR_0 values than any HPF operator and the GAS operator (the absolute value of the GRAD plus Gaussian-histogram reshaping) yields still better results.

From these data, we conclude that the HPF operator is inferior to the GRD one, even for non-pure MSI data. In Figure 5, we show three HP filtered versions of image S22 with increasing cut-off frequency f_0. As predicted, the edges of the image become more enhanced as f_0 is increased, but the image contrast decreases (i.e., the energy in the edges decreases).

Insert *

Table 8. Edge-enhancement operator tests (LTL data)

EXPERIMENT	INPUT-REF	SNR	COMMENTS
1	S22⊛S23	3.3	
2	S22.FIL2⊛S23.FIL2	9.7	HPF better than no preproc (not MSI)
3	S22.AFIL2⊛S23.AFIL2	8.0	Abs Value gives loss since not MSI
4	S22.GRD⊛S23.GRD	11.6	GRD better than HPF
5	S22.GAS⊛S23.GAS	13.1	GAS best of all
6	S22⊛S25	4.6	
7	S22.FIL3⊛S25.FIL3	11.7	HPF better than no preproc (not MSI)
8	S22.AFIL3⊛S25.AFIL3	6.3	Abs Value gives loss since not MSI
9	S22.GRD⊛S25.GRD	12.5	GRD better than HPF
10	S22.GAS⊛S25.GAS	16.5	GAS best of all

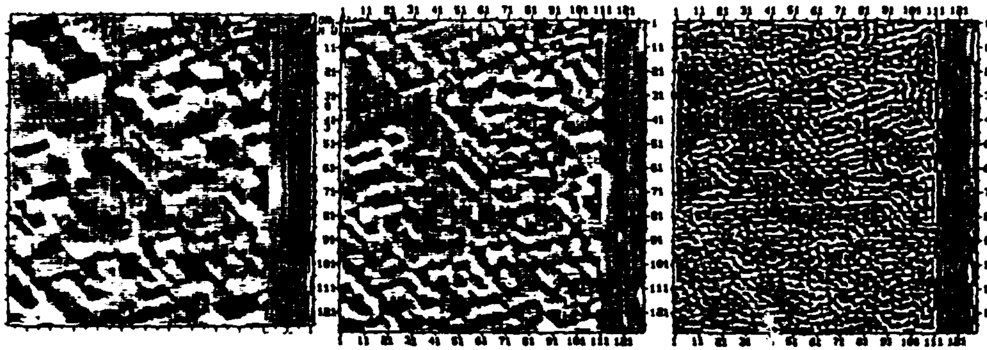

(a) S22.FIL1 (b) S22.FIL2 (c) S22.FIL3

Figure 5 Three filtered versions of image S22 with increasing cutoff frequency.

Similar experiments were performed on the SMS imagery with even more dramatic results (since this synthetic data was essentially pure MSI). The highlights are included in Table 9. From experiments one and two, we see that negligible SNR_0 occurs for the cross-correlation with no preprocessing (as is expected for MS data). A WIT (whitening) operator was also applied to this data. It gave excellent results for the auto-correlation (experiment three). Since this case corresponds to pure USI data, this result is expected. The much lower SNR_0 obtained with the WIT operator in cross-correlations (experiment four) verifies that whitening is not of use on pure MSI data. This experiment four also verifies that the image pair is uncorrelated and thus represents a pure MSI pair. From experiments five and six, we see that the HPF operator without the absolute value operator is of little use on pure MSI data. From experiment seven, we find that our special GAS operator provides much better SNR than does any other preprocessing operator.

Table 9. Edge-enhancement operator tests (SMS data)

EXPERIMENT	INPUT-REF	SNR	COMMENTS
1	SIM1⊛SIM1	6.3	
2	SIM1⊛SIM2	0.6	Low, thus nearly pure MSI
3	SIM1.WIT⊛SIM1.WIT	183	WIT helps pure USI (≡ auto-correl)
4	SIM1.WIT⊛SIM2.WIT	3.7	WIT not good for nearly pure MSI
5	SIM1.FIL3⊛SIM2.FIL3	2.3	}HPF without abs.value
6	SIM1.AFIL3⊛SIM2.AFIL3	15.8	} useless for nearly pure MSI
7	SIM1.GAS⊛SIM2.GAS	32.7	GAS excellent for nearly pure MSI

092-8

10. THRESHOLD SELECTION AS A FUNCTION OF SNR_i

In the major experiments performed on a pair of SMS data, zero-mean white Gaussian noise was added to one of the images to produce two SMS images with $SNR_i = 3$ and $SNR_i = 4$. Thresholded versions of these images with different thresholds were correlated with a GAS preprocessed version of the other image (with different gray level distributions). The resultant degradation SNR/SNR_0 in SNR_0 from the $SNR_i = \infty$ case (SNR_0) is plotted in Figure 6 versus the normalized threshold Th for the two SNR_i cases. Although these data were obtained for one isolated image correlation pair rather than the statistical ensemble necessary, the results agree quite well with those predicted by theory [13]. A clear peak in $D = SNR/SNR_0$ is observed for $Th \neq 0$, the optimum Th increases as SNR_i decreases, and the degradation becomes worse as SNR_i decreases. These experimental data suggest that our optimum Th parameter selection technique [13] is valid.

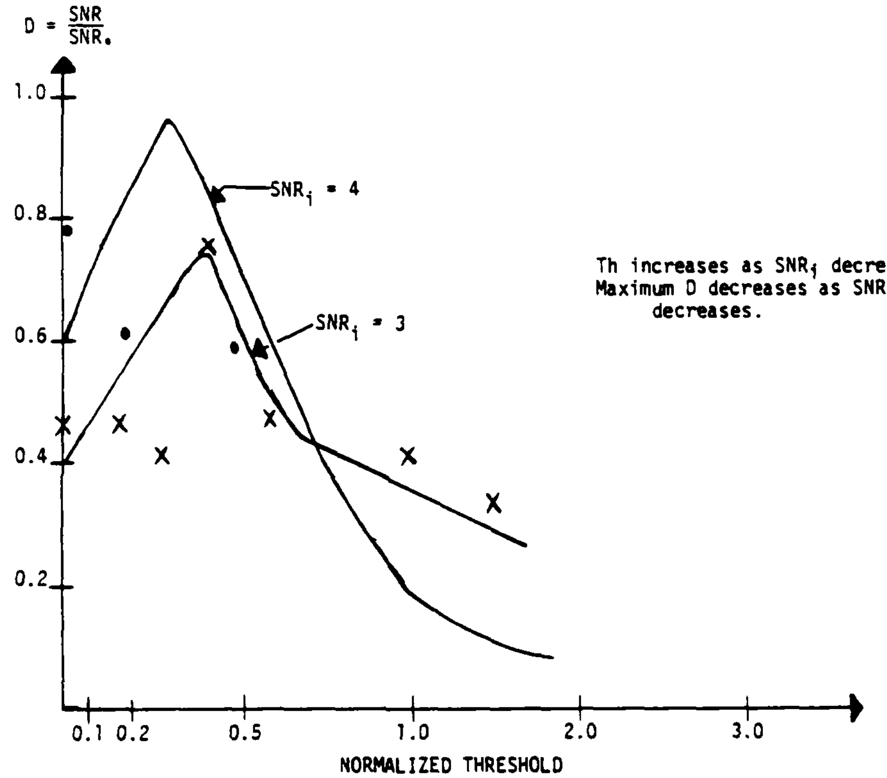

Figure 6 Experimentally determined degradation in SNR_0 from $SNR_i = \infty$ case (SNR_0) as a function of the normalized threshold for two different SNR_i values using SMS data.

11. SUMMARY AND CONCLUSIONS

In this paper, a new multisensor image model using random variables to represent the amplitude and location of the edges in an image was reviewed and experimentally verified. A general multisensor image pattern recognition processing architecture with a wide variety of preprocessing operators was also reviewed and the need for the various preprocessing operators was analyzed by experiments. The nonlinear polarization equalization operator and the Gaussian histogram reshaping operator had not been included in prior multisensor processors. Our experiments showed that the correlation coefficient ρ was a useful measure of whether an image pair was USI or MSI with $\rho > 0.5$-0.6 being indicative of USI data.

For MSI data, we showed that HPF was inferior to the GRD operator, that HPF without an absolute value operator was useless, that Gaussian histogram reshaping improved the output

292-18

correlation by an average of 15%. We verified the major theoretical remarks we advanced earlier [13] regarding how the number of independent objects in the image affects the data and moreso that our theory by which the optimal threshold can be selected was valid. These experimental verifications provided much insight into the nature of multisensor image pattern recognition.

ACKNOWLEDGEMENT

The support of the Air Force Office of Scientific Research (Contract 79-0091) under which a part of this work was performed at Carnegie-Mellon University is gratefully acknowledged.

REFERENCES

1. D. Casasent and D. Munoz, SPIE, 201, 58 (1979).
2. D. Casasent and Y. Barniv, SPIE, 137, 57 (1978).
3. P. Anuta, IEEE, GE-8, (October 1970).
4. M. Svedlow et al, IEEE, AES-14, (January 1978).
5. W. Pratt, IEEE, AES, (May 1974).
6. A. Rosenfeld et al, IEEE, C-21, (July 1972).
7. M. Kelly, Machine Intelligence, Chapter 22.
8. G. Vanderbrug and A. Rosenfeld, IEEE, C-26, (April 1977).
9. L. Novak, IEEE Conf on Decision and Control (1976).
10. R. Hudgin, "Image Matching Using Structure Information", Itek Corporation Report.
11. G. Robinson and J. Reis, "A Real-Time Edge Processing Unit", Northrop Research and Technology Center, IEEE Workshop, Chicago (1977).
12. R. Wong, IEEE, AES-14, (January 1978).
13. Y. Barniv et al, SPIE, 238, 156 (1980).
14. R. Wong, IEEE, SMC-7, (December 1977).
15. A. Arcese et al, IEEE, IT-16, (September 1970).
16. C. McGillem and M. Svedlow, IEEE, GE-14, 44 (1976).
17. C. McGillem and M. Svedlow, IEEE, GE-15, 257 (1977).
18. D. Casasent and A. Furman, Applied Optics, 16, 1652, 1662 (1977).

SECTION 6

INTRA-CLASS PATTERN RECOGNITION USING SYNTHETIC DISCRIMINANT FUNCTIONS

292-02

INTRA-CLASS IR TANK PATTERN RECOGNITION USING SDFs

Charles F. Hester* and David Casasent

Carnegie-Mellon University, Department of Electrical Engineering
Pittsburgh, Pennsylvania 15213
***Present Address: U.S. Army Missile Command,** DRSMI-REI
Redstone Arsenal, Alabama 35898

ABSTRACT

A hyperspace description of a matched spatial filter (MSF) correlator is advanced and used to develop a new MSF that is a synthetic discriminant function (SDF). The use of this filter to recognize objects independent of their aspect is described. Terminal homing recognition of tanks from IR imagery is taken as a case study. Bandpass filtering and a new maximum common information filter synthesis concept and issues such as filter energy are described and used to improve the system's intra-class pattern recognition ability and to overcome the intensity differences present in IR imagery. Experimental verification is also included.

1. INTRODUCTION

The recognition of the presence of a reference object in a cluttered background and the location of its position are old and familiar problems in pattern recognition [1]. Correlation of the on-line input image with a stored reference pattern is one of the more attractive solutions to such problems. This operation can be realized both optically (in a frequency plane correlator or in other architectures [2]) or digitally (using FFT algorithms [3]). However, in most practical pattern recognition problems, the input image and the reference function will differ due to intensity differences (this is especially prevalent when multisensor or IR imagery is used) and moreso due to geometrical differences (this problem is of major concern when the aspect angle from which the object is viewed cannot be controlled). Our specific pattern recognition case study concerns the recognition and location of M-60 tank targets from IR imagery. In this application, both geometrical and intensity differences exist between the input and reference data.

Because of the ease with which a correlation can be performed optically, we consider the use of a frequency plane correlator for this pattern recognition problem. However, since the performance of a correlator is well-known to seriously degrade when random contrast reversals [4] or geometrical distortions [5] exist, we suggest a hyperspace description of the data, the MSF and the correlator (Section 2) to overcome these problems. Using this hyperspace description, we develop a synthetic discriminant function (SDF) and use it as a synthetic MSF in our optical correlator. In Section 3, we review our prior [6,7] SDF approach in terms of this new hyperspace formulation. In Section 4, we review three techniques (Fourier transform kernels, Gram-Schmidt (G-S) techniques and Karhunen-Loeve (K-L) techniques) for basis function selection with emphasis on our new G-S method. When additive noise of zero-mean is present, modifications to the SDF synthesis procedure are required. These issues, derivation of the correlation SNR_0 in terms of hyperspace parameters and new concepts such as maximum filter energy and the maximum common information (MCI) filter are then developed in Section 5. Experimental verification and demonstration of this SDF approach to optical MSF pattern recognition are provided in Section 6. Our present attention lies with improving the intra-class pattern recognition performance of the system (i.e. the ability of the SDF to recognize different aspect views of the same reference object as members of the same class). In a companion paper [8], we consider extensions of these techniques for inter-class discrimination of tanks from other false targets and from non zero-mean background noise.

2. HYPERSPACE DESCRIPTION OF A MSF CORRELATOR

To provide a new filter function for use in a correlator that is capable of maintaining recognition of a reference object independent of geometrical distortions, we use an alternate hyperspace description of the input data and the filter function. We use 1-D functions for simplicity. Each of the members of the input data set $\{f_n(x)\}$ of objects to be recognized is written as an expansion in terms of the basis functions $\phi_m(x)$ and weighting coefficients a_m as

$$f(x) = \sum_m a_m \phi_m(x). \tag{1}$$

Each f in $\{f_n\}$ is plotted as a M-dimensional vector in an M-dimensional hyperspace with axes ϕ_m and with the projections on each axis being the a_m coefficients in (1). Thus, each input can be described as a vector

Casasent

$$\hat{f} = (a_1, a_2, \ldots, a_M). \tag{2}$$

The basis function set $\{\phi_m\}$ is orthonormal and different coefficients a_{nm} exist for the N different f_n members of the set $\{f_n\}$.

Two surfaces in hyperspace that are quite useful are the hypersphere and the hyperplane. A hypersphere of radius R_s is described by $\hat{f} \cdot \hat{f} = R_s$(a constant). This corresponds to an equi-energy surface. This can easily be seen from the definition of the energy ε_f of the function f as

$$\varepsilon_f = \int f^2(x)\, dx = \sum_m a_m^2 = \hat{f} \cdot \hat{f} = R_s. \tag{3}$$

A hyperplane also has physical significance as the product of two vectors (one of which g is fixed). It also corresponds to the correlation R_{fg} output of two functions f and g (evaluated at $\tau = 0$), i.e.

$$\varepsilon_{fg} = \hat{f} \cdot \hat{g} = \sum_m a_m b_m = \underline{a}\,\underline{b}^T = f \circledast g\big|_{\tau=0} = R_{fg}(0) = R_p. \tag{4}$$

In (4), we assume that both f and g are expanded in terms of the same $\{\phi_m\}$ basis set and that they have coefficence a_m and b_m respectively. The energy ε_{fg} in the output correlation, with no shift ($\tau = 0$) between f and g, is $R_{fg}(0)$. If g is fixed (i.e. if the b_m are fixed), then the $\hat{f} \cdot \hat{g} = R_p$(a constant) surface is a hyperplane. This describes the output of a correlator ($f \circledast g$) with the requirement that the correlation equal the constant R_p value.

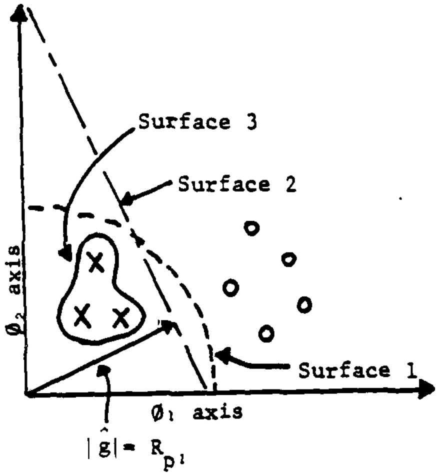

FIGURE 1. Simplified (2-axis) hyperspace pattern recognition problem

In our MSF correlation analogy, the fixed reference function $\hat{g}$ is our MSF $\hat{h}$. It corresponds to the vector drawn from the origin in hyperspace normal to the $\hat{f} \cdot \hat{g} = R_p$ hyperplane. This hyperplane describes the case of a constant output from the correlator. Any f in $\{f_n\}$ when correlated with $\hat{g}$, should lie on this hyperplane to be recognized. In Figure 1, we show a simple pattern recognition example for a M = 2-axis hyperspace. The X's are one class of objects to be recognized and the 0's are another class of objects to be separated. Surface 1 in Figure 1 describes a hypersphere with $R_s = R_{s1}$. Surface 2 describes a hyperplane corresponding to $R_p = |\hat{g}| = R_{p1}$. Surface 3 represents a more complex hypersurface. To recognize the X's and separate them from the object class 0, we can require $\hat{f} \cdot \hat{g} \le R_{p1}$ (surface 2) or $\hat{f} \cdot \hat{f} = \varepsilon_f \le R_{s1}$. Our major concern in this paper is how to select the $\{\phi_m\}$ to produce the excellent separation of the different object classes (inter-class pattern recognition) and the excellent clustering of the data for each class (intra-class pattern recognition) shown in this simplified example in Figure 1. The presence of noise in the data will appear centered at the origin in hyperspace as well as around the hyperplane. In these cases more advanced techniques (Sections 3-5) are required.

3. SYNTHETIC DISCRIMINANT FUNCTION (SDF) SYNTHESIS

In this section, we describe our general synthetic discriminant function synthesis technique and how it is used within our hyperspace description of a MSF pattern recognition correlator. We write the $\hat{f}_n$ members of our training set $\{f_n\}$ of input objects to be recognized

292-02

as

$$\hat{f}_n = \sum_m a_{nm} \hat{\phi}_m. \tag{5}$$

We denote our desired filter function by $\hat{h}$. We write it as a similar expansion in the same $\{\phi_m\}$ basis set as

$$\hat{h} = \sum_m b_m \hat{\phi}_m. \tag{6}$$

We require the correlation of all $\hat{f}_n$ with $\hat{h}$ to equal a constant R_p. When the $\hat{\phi}_m$ are orthonormal, this condition reduces to

$$\hat{f}_n \cdot \hat{h} = R_{f_n h}(0) = \sum_m a_{nm} b_m = R_p = \text{constant}. \tag{7}$$

Our pattern recognition problem can now be stated quite simply. We desire to find the filter function $\hat{h}$ in (6) that satifies (7) for all f in the training set $\{f_n\}$. To do this, we must determine the b_m and the ϕ_m. Four steps are required to achieve this. We first form the autocorrelation matrix

$$\underline{R}_{f_i f_j}(0) = \hat{f}_i \cdot \hat{f}_j. \tag{8}$$

of all $\hat{f}_n$ inputs. We then diagonallize the $\underline{R}$ matrix in (8). Techniques to do this are described in Section 4. This yields the $\hat{\phi}_m$. We then determine the a_{nm} coefficients in (5) from

$$a_{nm} = \hat{f}_n \cdot \hat{\phi}_m. \tag{9}$$

To find the b_m, we pick the constant R_p in (7) (in this paper we arbitrarily select $R_p = 1$) and use the a_{nm} found from (9) in (7). We then know the ϕ_m and the b_m and hence can form the filter $\hat{h}$ in (6) with the necessary correlation feature in (7).

4. BASIS FUNCTION SELECTION

Let us now elaborate on the various techniques by which the $\{\phi_m\}$ basis function set can be determined from the autocorrelation matrix $\underline{R}$ in (8). One of the simplest orthonormal basis function sets are the Fourier kernel functions. Duvernoy [9-12] and Caulfield [13-14] have used these in analogous SDF synthesis. However, details of the steps involved in their filter synthesis and how the Fourier coefficients to be retained were chosen have not been provided. Moreso, they selected quite specific pattern recognition problems for which the Fourier coefficients appear to represent an attractive basis set for data discrimination. Our concern is to develop a more general and organized approach to basis function selection rather than relying on ad hoc techniques and use of a fixed (Fourier kernel) basis set that might not always be best for a given general pattern recognition problem.

In [6,7], we developed a new G-S technique for generation of a general basis function set. The algorithm is described by

$$\left.\begin{aligned}
\phi_1 &= f_1(x)/E_1 \\
\phi_2 &= [f_2(x) - Z_2(r_{21})\phi_1(x)]/E_2 \\
&\ \vdots \\
\phi_m &= [f_m(x) - \sum_{\ell=1}^{m-1} Z_m(r_{m\ell})\phi_\ell(x)]/E_m \\
&\ \vdots \\
\phi_M &= [f_M(x) - \sum_{\ell=1}^{M-1} Z_M(r_{m\ell})\phi_\ell(x)]/E_M
\end{aligned}\right\} \tag{10}$$

where $R_{ij} = \hat{f}_i \cdot \hat{f}_j$ are the elements of the autocorrelation matrix $\underline{R}_{f_i f_j}$.

$\hat{\phi}_m = \sum_{n=1}^{m} d_{mn} \hat{f}_n$ can be used to describe the m-th basis function as a function of the m-th input f_m and the prior f_ℓ inputs ($\ell \leq m - 1$).

$Z_m = \sum_{k=1}^{m} d_{mk} r_{k\ell}$ describes the weighting functions in (10) applied to the $\ell = m - 1$ previously computed basis functions ϕ_ℓ and where d_{mk} is found as above.

292-02

$E_m = \{\int [f_m(x) - \sum_{\ell=1}^{m-1} z_m(r_{m\ell}) \phi_\ell(x)]^2 dx\}^{1/2}$ is the energy normalization constant.

From (10), we note that in our G-S procedure: ϕ_1 depends only on f_1, the weighted and normalized contribution of f_1 is subtracted from f_2 and thus ϕ_2 depends only on f_2 and moreso it contains the f_2 data not present in f_1, similar remarks apply to ϕ_m in terms of f_{m-1} and f_m. Thus, our G-S procedure decorrelates the $\{f_n\}$ input data set. Moreso, in many cases $M > N$, in which case our G-S procedure is quite attractive since it forces $M = N$ without the need for the use of an ad hoc technique to selectively remove $M - N$ basis functions. We also note that a different $\{\phi_m\}$ basis set will result if a different ordering of the $\{f_n\}$ is used and that for each new ordering of the $\{f_n\}$ a new $\hat{h}$ will result. However, for a fixed $\{f_n\}$ data set, all $\hat{h}$ will correspond to the same hyperplane in a rotated hyperspace version of the original space. This property follows directly from the fact that a unitary transformation does not change the relative distances between points on a hyperspace. We conclude by noting that the output correlation $R_{fh}(0)$ is evaluated at $\tau = 0$, and that this corresponds to the case of no shift between the input and the reference function not to the value of the correlation at its maximum peak location. We also remind the reader that a shifted (translated) version of any input function $\hat{f}_n$ represents a new input function and will result in a new $\{f_n\}$ input data set and a new $\hat{h}$ filter. In Section 5, we use these last two observations in the design of a maximum common information (MCI) filter to improve the correlation plane SNR_0 performance of our SDF pattern recognition processor.

K-L techniques [15-16] can also be used to diagonalize a matrix such as $\underline{R}$ in (8). We consider this approach in more detail in [8]. For now, we only note that it requires an adequate statistical ensemble and that it provides the optimal basis set of reduced dimensionality. This can greatly expedite the off-line calculations necessary to generate the SDF function $\hat{h}$.

In this paper, we will concentrate on the use of the G-S technique in (10) to determine the SDF function $\hat{h}$ to satisfy (7) for the intra-class pattern recognition problem of present concern. The procedure, notation and terminology we use follow. Diagonalization of $\underline{R}$ in (8) yields a set of equations for the ϕ_m in terms of the f_n

$$\hat{\phi}_m = \sum_n d_{mn} \hat{f}_n. \tag{11}$$

We denote the matrix with element values d_{mn} in (11) as the G-S coefficient matrix. Solving (11), we obtain an expression for the original $\hat{f}_n$ inputs in terms of the $\hat{\phi}_m$ basis functions as in (5). We denote this matrix with elements a_{nm} in (5) as the target matrix, $\underline{F}_T$ (or $\underline{F}_{TGS}$ if the G-S diagonalization technique is used). The equal output correlation requirement in (7) can then be written in terms of $\underline{F}_T$ as

$$\underline{F}_T\hat{h} = R_p\hat{u}, \tag{12}$$

where $\hat{u}$ is the unit vector. Computing the inverse target matrix $\underline{F}_T^{-1}$ (by Gaussian elimination or other techniques), applying $\underline{F}_T^{-1}$ to (12) and recalling that $\underline{F}_T^{-1}\underline{F}_T = \underline{I}$ (the identity matrix), we find the expression from which $\hat{h}$ can be obtained is

$$\hat{h} = \underline{F}^{-1}R_p\hat{u}. \tag{13}$$

This gives $\hat{h}$ in terms of $\hat{\phi}_m$. Substituting (11) into (13) we obtain the equation from which we can determine $\hat{h}$ from the elements of the original input set $\{f_n\}$. The above notation and terminology and specific forms for the various matrices will be provided in our experimental data (Section 6).

5. ADDITIVE (ZERO-MEAN) NOISE EFFECTS

We now consider the effect of zero-mean additive noise on the selection of the SDF and the performance of our synthetic MSF correlator. We desire a new correlation plane SNR_0 expression and will present a simplified hyperspace model of this case. We then discuss a new maximum common information (MCI) filter concept we use to improve the performance of the processor. The assumption of zero-mean noise is realistic since the mean of the data is removed in the digital processing of IR data and because such filtering directly occurs in optical MSF synthesis. We will consider the case of colored noise, background noise with non-zero mean value and false targets in [8].

The noisy input is $\hat{f}' = \hat{f} + \hat{n}$, where $\hat{n}$ is the noise vector with elements n_n that are random and independent with a variance σ^2_{nn}. Since the mean $\langle n \rangle$ of the noise is zero, its average energy $\varepsilon_{n\,avg} = \langle \hat{n} \cdot \hat{n} \rangle = \sum_n \sigma^2_{nn}$ and we can thus bound the noise by the hypersphere at

Casasent

the origin of radius $\rho = K<\hat{n} \cdot \hat{n}>^{1/2}$, where the constant K is determined by the confidence with which we know the variance of the noise. Since $<\hat{f}'> = \hat{f}$, we can similarly bound $\hat{f}'$ to lie within a sphere of radius $r = |\hat{n}|$ of $\hat{f}$. We thus modify our correlation threshold criteria *in* (7) *to be* $\hat{f}_n' \cdot \hat{h} = R_p \pm r$ to include the effects of noise. The corresponding hyperspace diagram of Figure 2 helps to show these issues under simplifying conditions such as no attention to the distribution of $\hat{n}$ within the sphere at the origin and with no attention to devising the optimal filter $\hat{h}$ for a specific noise distribution.

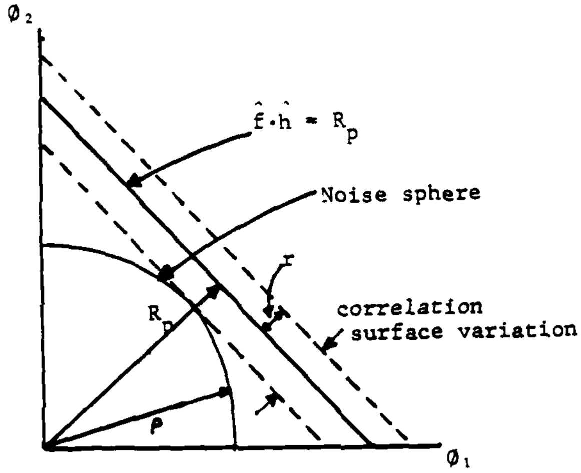

FIGURE 2. Simplified hyperspace model showing the effects of additive noise

An appropriate SNR_0 measure for the output correlation plane pattern is thus

$$SNR_0 = K = \frac{\rho}{<\hat{n} \cdot \hat{n}>^{1/2}} = \frac{(\epsilon_h^{1/2} - r)}{<\hat{n} \cdot \hat{n}>^{1/2}} = \frac{0.5\epsilon_h^{1/2}}{<\hat{n} \cdot \hat{n}>} . \tag{14}$$

In (14), we have noted that $\rho \leq \epsilon_h^{1/2} - r$ must be satisfied to avoid overlap in Figure 2. From an analysis of the probability of correct registration P_C and using Bayesian logic, we find that the optimum choice for r and ρ is $r = 0.5\epsilon_h^{1/2} = \rho$. This maximizes P_C and both the probability with which the *noise* is bounded within ρ at the origin and within r of the $\hat{f}_n \cdot \hat{h}$ hyperplane. From (14), we see that maximizing the energy ϵ_h of the filter and/or reducing the noise variance $<\hat{n} \cdot \hat{n}>$ will improve the performance of the filter. We now investigate the use of a new MCI technique and bandpass filter (BPF) preprocessing to achieve improved SDF performance.

We can show that an upper-bound ϵ_{hUB} on the energy of the filter is $\epsilon_m = \epsilon_{f_m}$ (the energy of the minimum energy input function f_m in the input data set) and that a lower-bound $\epsilon_{hLB} = 1/(N <1/\epsilon_n>)$, where $<1/\epsilon_n>$ is the average reciprocal energy in the input data set. We have also shown that if any pair of inputs $\hat{f}_i$ and $\hat{f}_j$ in $\{f_n\}$ correlate, then ϵ_h will be increased. We use this observation and our remarks in Section 4 on the G-S technique to optimally shift all of the $\{f_n\}$ inputs to maximize their cross-correlation, thereby increasing ϵ_h. Since this operation aligns and maximizes the common information in the input data set, we refer to this technique as MCI and we call the resultant $\hat{h}$ an MCI filter. Since any one shifted version of one target aspect need be included in our input set to enable all shifted versions of that aspect to be recognized by the resultant filter (the shift-invariant feature of the Fourier transform MSF correlator insures this), we can simply select the shifted input that maximizes the filter energy and hence the output SNR in (14).

A preprocessing operation that we applied prior to selection of the basis functions and the MCI filter is a bandpass filter (BPF). This technique was described earlier [6,7] and thus is not repeated here. We note only that its use is quite appropriate for IR pattern recognition where the *mean* value is not reliable and where high spatial frequency data is noise. This operation decreases the variance of the noise and maximizes the SNR_0 in (14).

6. EXPERIMENTAL VERIFICATION

To apply the SDF, MCI and BPF pattern recognition techniques, we chose the problem of recognizing an M-60 tank independent of its aspect from input IR imagery. This terminal homing missile guidance problem thus incorporates both intensity and geometrical differences between the input and reference data. As our training set, we used seven IR images of an M-60 tank, each being a different aspect view of the target. A representative set of these images and their digitized versions (128x128 pixels) are shown in Figure 3.

f_1 - Right Side (RS)

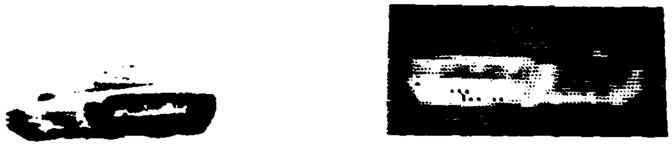

f_3 - Front/Side (F/S)

f_4 - Rear (R)

FIGURE 3. Selected input imagery in $\{f_n\}$ (left) and their digitized reconstructions (right).

As described in Section 5 and references [6,7], optical weighted MSF synthesis was used to determine the optimal BPF to use. This BPF was then applied to the input data set to improve the correlation plane SNR_0 in (14). The correlation planes for all 49 image pair correlations were then obtained and the locations of three largest correlation peaks in each of the 21 upper off-diagonal $R_{f_i f_j}$ correlation plane patterns were noted. A sequential technique was used to investigate the filter energy ε_h corresponding to each of the $2 \cdot 3 (N - 1)! = (66)! = 4320$ possible input shift cases. The combination of shifted inputs with the maximum filter energy ε_h was then selected as our input data set $\{f_n\}$. *The autocorrelation* matrix for this MCI input set $\{f_n\}$ is shown in Table 1. The G-S *coefficient* matrix obtained from Table 1 using *(10) is* shown *in* Table 2.

The SDF filter $\hat{h}$ that results from applying the procedure in (11)-(13) *is shown in Figure* 4. In Figure 5, we show five cross-sectional scans taken at one pixel intervals through the auto-correlation output for input image f_3 and the cross-correlation output $\hat{f}_3 \cdot h$ of this image and the MCI SDF filter $\hat{h}$. From Figure 5, we see that the shape and width of the output correlation is preserved quite well by our MCI SDF reference MSF filter.

292-02

Aspect / Aspect	1	2	3	4	5	6	7
1	14.5	6.2	4.6	-0.1	3.2	4.6	-3.4
2	6.2	16.2	5.5	-0.4	4.0	6.4	-0.5
3	4.6	5.5	36.7	3.1	8.8	5.6	1.5
4	-0.1	-0.4	3.1	11.7	0.2	0.2	3.2
5	3.2	4.0	8.8	0.2	31.2	4.9	1.5
6	4.6	6.4	5.6	0.2	4.9	18.8	-0.5
7	-3.4	-0.5	1.5	3.2	1.5	-0.5	7.6

Table 1. Auto-correlation matrix

Aspect / basis	1	2	3	4	5	6	7
ϕ_1	0.262						
ϕ_2	-0.074	0.257				0	
ϕ_3	-0.059	-0.031	0.172				
ϕ_4	-0.033	0.018	-0.005	0.294			
ϕ_5	-0.072	-0.023	-0.005	0.008	0.187		
ϕ_6	-0.015	-0.054	-0.025	0.026	-0.026	0.246	
ϕ_7	-0.011	-0.014	0.001	-0.039	-0.007	0.007	0.367

Table 2. Gram-Schmidt coefficient matrix

INPUT IMAGE NUMBER	1	2	3	4	5	6	7
I_p (relative units)	7.89	7.60	7.15	7.51	7.82	7.91	7.29

Table 3. Peak intensities for the correlations of inputs $\hat{f}_1$ to $\hat{f}_7$ with $\hat{h}$

292-02

FIGURE 4. The maximum common information (MCI) synthetic discriminant function (SDF) filter $\hat{h}$ obtained by the Gram-Schmidt (G-S) procedure.

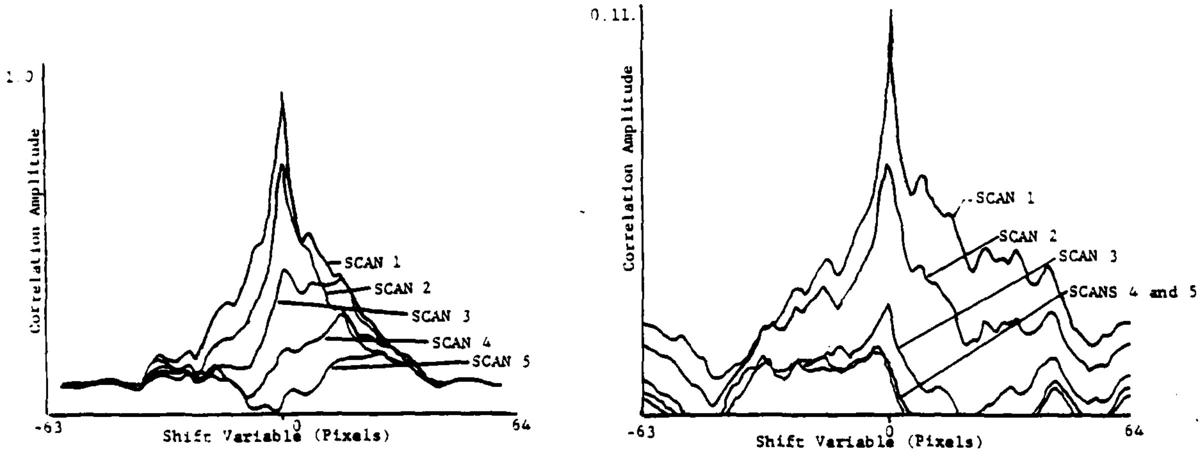

(5a)

(5b)

FIGURE 5. Cross-sectional scans through the autocorrelation of $\hat{f}_3 \cdot \hat{f}_3$ (Figure a) and the cross-correlation $\hat{f}_3 \cdot \hat{h}$.

Carasent 6

292-02

In Table 3, we list the peak correlation values I_p obtained from the correlations of $\hat{h}$ in Figure 4 with all seven input tank aspects $\hat{f}_1$-$\hat{f}_7$ (see Figure 3). We find all seven I_p values to be equal within 5% as predicted from (7). The small differences observed are due to sampling and roundoff errors. In view of the fact that the one SDF can recognize all different aspect views of the target, the variations in Table 3 are negligible. The desired performance of our MCI SDF filter has thus been demonstrated. By inspection of Figure 4, we see that the filter function $\hat{h}$ exhibits quite significant structure. We thus expected to exhibit considerable discrimination [8] for inter-class pattern recognition as well as good intra-class recognition of different aspect views of the same object (the case considered herein).

SUMMARY AND CONCLUSIONS

In this paper, we have shown how to formulate the conventional matched spatial filter correlator in terms of a new hyperspace representation. We have also included the case of additive zero-mean noise in our analysis. This representation leads to a new synthetic discriminant function matched filter capable of recognizing a reference object independent of the input image aspect view used. The use of bandpass filter preprocessing to enhance the filter's performance on IR and multisensor imagery was noted and demonstrated. A new maximum common information filter concept was developed to enhance the correlation SNR_0 by increasing the filter's energy. Experimental verification on infrared M-60 tank imagery was included to demonstrate the new theoretical concepts described. With one synthetic discriminant function filter, we were able to successively correlate and recognize all aspect views of the input object with essentially identical output peak intensity and SNR values. The problem and application were selected so that off-line filter synthesis was realistic. Methods to decrease the computational load and storage requirements of this off-line filter synthesis process are the subject of current research.

ACKNOWLEDGEMENTS

The support of this research by the Air Force Office of Scientific Research (Grant AFOSR 79-0091) is gratefully acknowledged as is the support of C.H. by MIRADCOM during his stay at Carnegie-Mellon University.

REFERENCES

1. Proc IEEE, 67, Special Issue on Pattern Recognition (May 1979).
2. D. Casasent, Proc IEEE, 67, 803 (1979).
3. W. Pratt, Digital Image Processing, Wiley, New York (1978).
4. Y. Barniv et al, SPIE, 238, 156 (1980) and SPIE, 292 (1981).
5. D. Casasent and D. Psaltis, Proc IEEE, 65, 77 (1977).
6. C. Hester and D. Casasent, SPIE, 201, 77 (1979).
7. C. Hester and D. Casasent, Applied Optics, 19, 1758 (1980).
8. C. Hester and D. Casasent, SPIE, 302 (1981).
9. J. Duvernoy, Applied Optics, 15, 1584 (1976).
10. J. Baures and J. Duvernoy, Applied Optics, 17, 3395 (1978).
11. J. Duvernoy, Applied Optics, 18, 2737 (1979).
12. J. Duvernoy and J. Leger, Optics Communications, 32, 39 (1980).
13. H. Caulfield and R. Haimes, SPIE, 201, 115 (1979).
14. H. Caulfield, Applied Optics, 19, 3877 (1980).
15. S. Watanabe, Trans Fourth Prague Conf, C19, 635 (1965).
16. K. Fukunaga and W. Koontz, IEEE, C19, 635 (1970).

SECTION 7

INTER-CLASS DISCRIMINATION USING SYNTHETIC DISCRIMINANT FUNCTIONS

302-17

INTER-CLASS DISCRIMINATION USING SDFs

Charles F. Hester* and David Casasent
Carnegie-Mellon University, Department of Electrical Engineering
Pittsburgh, Pennsylvania 15213
*Present Address: U.S. Army Missile Command, DRSMI-REI
Redstone Arsenal, Alabama 35898

ABSTRACT

A hyperspace formulation of matched spatial filter pattern recognition together with bandpass filter preprocessing leads to synthesis of a synthetic discriminant function that can recognize a reference object independent of intensity and geometrical differences between inputs. Use of a maximum common information preprocessing concept, Karhunen-Loeve techniques, non-unitary transformations with multi-channel synthetic discriminant functions and a new decorrelation transformation to provide inter-class discrimination for our synthetic discriminant function system are considered. Experimental verification on M-60 tank targets and an armored personnel carrier false target are included.

1. INTRODUCTION

The recognition of the presence of a reference object in a cluttered background and the location of its position are the classic problems in pattern recognition [1]. One of the more attractive solutions to such problems is to correlate the on-line input image with a stored reference pattern. The correlation operation can be realized both optically [2] and digitally [3]. Our present concern is the fact that in most practical pattern recognition problems, the input image and the reference function will differ due to intensity variations (this occurs when multisensor or infrared imagery is used) and moreso due to geometrical differences that arise (especially when the aspect angle from which the object is viewed cannot be controlled). Our specific pattern recognition case study concerns the recognition and location of tank targets from IR imagery and the discrimination of these target objects from false targets such as trucks and armored personnel carriers. In this application, both geometrical and intensity differences exist between the input and reference data.

Because of the ease with which a correlation can be performed optically, we consider a new hybrid optical/digital pattern recognition system. This processor uses bandpass filter (BPF) preprocessing, an optical correlator and a synthetic discriminant function (SDF) as the matched spatial filter (MSF) reference. The SDF $\hat{h}$ is synthesized off-line from a training set containing N different aspect views $\{f_n\}$ of the reference object. A hyperspace description of the data base, MSF and output correlation was used in [4] to develop an SDF capable of recognizing a reference object independent of its aspect view. Because the performance of a correlator rapidly degrades with even simple geometrical distortions between the input and the reference object [5], use of an SDF and a hyperspace description of a pattern recognition problem is most useful. It also represents a new, attractive and practical approach to optical pattern recognition when severe geometrical distortions (such as different aspect views of the object) must be handled.

In [6,7], a Gram-Schmidt (G-S) technique for SDF synthesis and the use of BPF preprocessing for the case of IR input imagery was described. In [4], we described our hyperspace formulation of a MSF correlator and introduced a new maximum common information (MCI) filter synthesis concept. In this paper, we consider advanced techniques to provide improved discrimination performance of these SDFs for inter-class pattern recognition applications. We briefly review our hyperspace formulation (Section 2) and our SDF synthesis technique together with details of the G-S and Karhunen-Loeve (K-L) methods (Section 3). The MCI concept together with its use in aligning common image structure is described in Section 4 with emphasis on the improved discrimination performance this operation provides. Two multi-channel SDF systems for inter-class discrimination are highlighted in Section 5. A new general decorrelation transformation and its use in inter-class discrimination are described in Section 6. These latter systems utilize non-unitary transformations to provide dimensionality reduction of the area (volume) of the discriminant hypersurface. Experimental verifications are included in Sections 4 and 6.

We distinguish three types of noise for which we desire increased discrimination. These include: additive zero-mean noise (the use of a BPF and a MCI filter is quite useful for this case [4]); color background noise with non-zero-mean and with a deterministic nature; and false targets. A K-L technique (Section 6) and a modified G-S technique using a decorrelation transformation (Section 6) are found to provide quite excellent discrimination for these latter two types of noise and false targets.

Casasent

2. HYPERSPACE DESCRIPTION OF A MSF CORRELATOR

We consider N input images $\{f_n\}$, each corresponding to a different aspect view of a reference object. We describe them by

$$f_n = \sum_{m=1}^{M} a_{nm} \phi_m, \tag{1}$$

where the ϕ_m are basis functions in the set $\{\phi_m\}$ and the coefficients a_{nm} are the elements of the target matrix F_T. We desire to determine an SDF filter function $\hat{h}$, which we write as a similar expansion in terms of the same basis function set as

$$h = \sum_{m=1}^{M} b_m \phi_m, \tag{2}$$

such that the correlation $R_{f_n h}$ of an f_n and h equals a constant. We describe h and the f_n as M-dimensional vectors $\hat{h}$ and $\hat{f}_n$ in an M-dimensional hyperspace whose axes are the basis functions ϕ_m and the coefficients of the vectors are their projections on the ϕ_m axes, e.g.

$$\hat{f} = (a_1, a_2, \ldots, a_M). \tag{3}$$

We can write our correlation condition, $f \circledast h = \text{constant}$, as

$$\hat{f}_n \cdot \hat{h} = \sum_m a_{nm} b_m = \underline{a}\,\underline{b}^T = f \circledast h \Big|_{\tau=0} = R_{fh}(0) = R_p. \tag{4}$$

The condition $\hat{f}_n \cdot \hat{h} = R_p$ = *constant in* (4) describes a hyperplane (if $\hat{h}$ is fixed). Specifically, the MSF or SDF $\hat{h}$ is a vector from the origin in hyperspace normal to the $\hat{f}_n \cdot \hat{h} = R_p$ hyperplane surface. If *any input* f *satisfies* (4), then *we* say that it is a member of the set $\{f_n\}$ of true targets. The energy of the function f is defined as

$$\varepsilon_f = \int f^2(x)\, dx = \sum_m a_m^2 = \hat{f} \cdot \hat{f} = R_s. \tag{5}$$

If $\varepsilon_f = \hat{f} \cdot \hat{f}$ equals a constant R_s as in (5), then this describes a hypersphere or an equi-energy surface in hyperspace. Hyperplanes and hyperspheres represent two quite useful and easily described and realizable dot product functions of use in pattern recognition.

3. SYNTHETIC DISCRIMINANT FUNCTION (SDF) SYNTHESIS

In this section, we highlight how the filter $\hat{h}$ in (2) that satisfies (4) for the input set $\{f_n\}$ in (1) can be derived [4,6,7]. We first form the autocorrelation matrix

$$\underline{R}_{f_i f_j}(0) = \hat{f}_i \cdot \hat{f}_j \tag{6}$$

of all $\hat{f}_n$ input image pairs. We then diagonalize $\underline{R}$ using G-S [4] or K-L [8,9] techniques. This yields the $\hat{\phi}_m$ as

$$\hat{\phi}_m = \sum_n d_{mn} \hat{f}_n, \tag{7}$$

where the d_{mn} are the elements of the G-S coefficient matrix. The target matrix $\underline{F}_T$ and its elements a_{mn} in (1) are found from the solution of (7). We write (4) as

$$\underline{F}_T \hat{h} = R_p \hat{u}, \tag{8}$$

where $\hat{u}$ is the unit vector. We compute the inverse target matrix $\underline{F}_T^{-1}$ and apply it to (8) to obtain

$$\hat{h} = \underline{F}_T^{-1} R_p \hat{u}, \tag{9}$$

Substituting (7) into (9), we find $\hat{h}$ in terms of the original input set $\{f_n\}$ of images.

Our G-S algorithm [4] to obtain the $\{\phi_m\}$ from the $\{f_n\}$ is described by

502-17

$$\left.\begin{aligned}\phi_1 &= f_1(x)/E_1\\ \phi_2 &= [f_2(x) - Z_2(r_{21})\phi_1(x)]/E_2\\ &\vdots\\ \phi_m &= [f_m(x) - \sum_{\ell=1}^{m-1} Z_m(r_{m\ell})\,\phi_\ell(x)]/E_m\end{aligned}\right\} \qquad (10)$$

In (10), Z_m is a function of the elements of the autocorrelation matrix r_{ij} (it describes the weighting to be applied to the previously computed basis functions) and E_m is an energy normalizing constant.

A K-L matrix diagonalization technique [8,9] can also be used to determine the $\{\phi_m\}$. In this technique, an ensemble average matrix

$$\underline{R} = E_n\{a_{nm}a_{nm}\} \qquad (11)$$

is formed where the a_{nm} are the coefficients of the $f_{n\phi}$ elements of $\{f_n\}$ in any orthonormal basis set ϕ_m and where the ensemble average is formed over the image index n (i.e. over all input imagery). A transformation $\underline{T}$ is applied to $\underline{R}$ to form the diagonal matrix

$$\underline{R}_D = \underline{T}^{-1}\underline{R}\,\underline{T}. \qquad (12)$$

This transformation produces new inputs $\hat{f}_{nKL} = \hat{f}_{n\phi}\underline{T}$ and new basis functions $\hat{\phi}_{mKL} = \hat{\phi}_m\underline{T}$ that satisfy

$$\underline{R}\hat{\phi}_{mKL} = \lambda_m\hat{\phi}_{mKL}, \qquad (13)$$

i.e. $\hat{\phi}_{mKL}$ are the eigenvectors of $\underline{R}$ and the λ_m are the eigenvalues.

Use of a Fourier kernel basis function set is also possible as the Fourier transform can easily be obtained optically and digitally. However, use of this basis set is quite restrictive. Its main function occurs in BPF processing. The G-S and K-L techniques are far more orgainized and less ad hoc and less restrictive. They directly provide the best basis function set for the input training data given. In the G-S technique, the basis ϕ_1 is a function only of f_1, the basis ϕ_2 is a function only of f_2 (with the part of f_2 contained in f_1 removed), etc. This operation of decorrelation of the input data performed by the G-S expansion will prove quite useful in our decorrelation transformations (Section 6) for improved SDF descrmination performance. The K-L technique is superior in terms of dimensionality reduction. Each basis function in the K-L expansion is a function of all inputs in $\{f_n\}$. Thus, we can order the $\hat{\phi}_{mKL}$ in terms of decreasing eigenvalues λ_m. By retaining only those basis functions with the largest eigenvalues, a quite reduced dimensionality problem results. In practice, three eigenvectors are adequate to describe and represent over 95% of the data in $\{f_n\}$. In Section 6, we combine these features of K-L and G-S expansions into a new image discrimination technique.

4. DISCRIMINATION PERFORMANCE OF THE MCI SDF FILTER

In [4], we used an image data base consisting of seven inputs of an M-60 tank taken from different aspects. We applied a BPF to the data (with the bandpass determined by optical weighted MSF synthesis as in [6,7]). We then operated on this BPF data base to increase its common information.

To see the reason for this, we recall from [4] that the SNR_0 of the output correlation is described by

$$SNR_0 = \frac{0.5\epsilon_h^{1/2}}{\langle\hat{n}\cdot\hat{n}\rangle^{1/2}} \qquad (14)$$

where ϵ_h is the energy of the filter $\hat{h}$ and where the denominator is the variance of the input noise (assumed to be zero-mean additive Gaussian noise). From (14), we note that increasing ϵ_h increases the SNR_0. In [4], we also noted that if the correlation $R_{f_i f_j}$ between any two elements of $\{f_n\}$ is increased, so is the filter's energy. From Section 2, we note that a shifted or translated version of any input corresponds to a new input, a new hyperspace vector and that a new $\hat{h}$ results for each such shifted input. From Section 3, we note that

Casasent 3

if the input set $\{f_n\}$ is fixed, then the same $\hat{h}$ will result regardless of the basis set used. Moreso, any one translated input can be used to recognize all translated versions of a given target aspect (because of the shift-invariance of a Fourier transform correlator).

From these considerations, we proceeded to optimally shift all input image pairs to maximize their common information and hence their cross-correlation. The resultant MCI input image set was obtained. Its auto-correlation matrix was produced. Its G-S coefficient matrix computed from (10) and $\hat{h}$ calculated from (7) and (9). This $\hat{h}$ MCI SDF filter (Figure 1) was found to yield nearly equal output correlations (within 5%) with all aspects of the reference M-60 tank object. By inspection of Figure 1, we see that this $\hat{h}$ has considerable structure and that it is not a blurred average of all of the inputs. Thus, we expected to provide good discrimination for inter-class pattern recognition (distinguishing true M-60 targets f_t from false targets f_f).

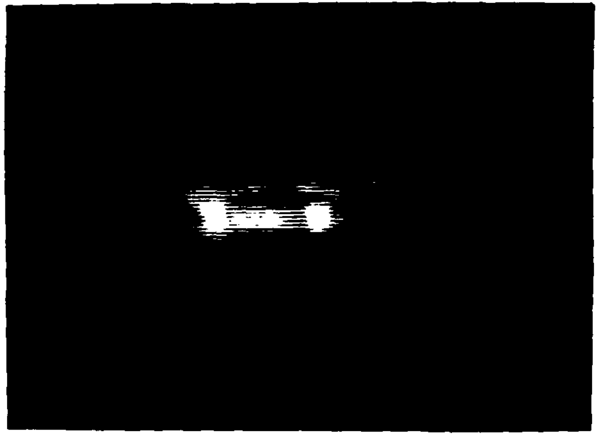

FIGURE 1. Synthetic discriminant function (SDF) produced by the maximum common information (MCI) technique.

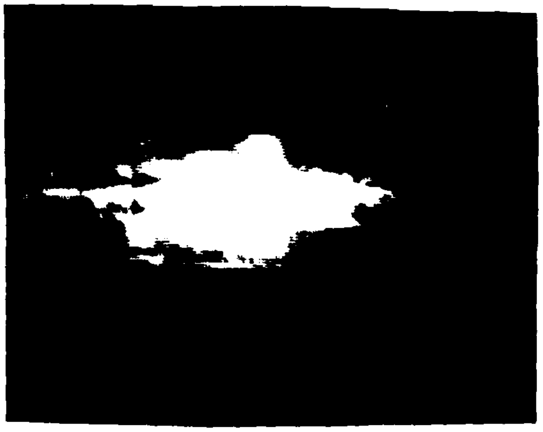

FIGURE 2. Synthetic discriminant function (SDF) produced by colocating the centroids of the input image set.

To pursue this observation, we formed a second $\hat{h}$ filter from the same BPF image set by colocating the centroids of the imagery (Figure 2). This represents a good initial estimate of the proper shifts necessary for the input data. From an analysis of the autocorrelation matrices for the MCI and the centroid colocated imagery, we found that the sum of the off-diagonal elements was increased by over 20% for the MCI data set. The peak intensity of the correlation outputs obtained showed about a 15% increase in the filter energy. We do not expect these two measures to be the same, but the increased filter energy and hence the increased SNR_0 obtained with the MCI filter is clearly apparent from this experiment.

Comment 4

302-17

We expect the major benefit from the MCI filter to come from its enhanced discrimination. To investigate this, we compare Figures 1 and 2. Although the centroid filter in Figure 2 appears to have more structure than the MCI filter in Figure 1, this is quite misleading, since a much higher exposure was necessary to photograph Figure 2 than Figure 1 and since much of the added "structure" present in Figure 2 is present because the image pairs were not properly aligned. Thus, in Figure 2, the added structure is of low intensity, whereas all intensities in Figure 1 are much higher than those in Figure 2. In addition, much more lower intensity structure is actually present in Figure 1 (but it is not visible because of the low dynamic range of the available display used to produce these figures).

IMAGE	1	2	3	4	5	6	7	
1	1.0	0.40	0.19	−0.00	0.15	0.27	−0.00	
2		1.0	0.22	−0.02	0.17	0.36	−0.04	
3			1.0	0.14	$\boxed{0.57}$	0.46	0.08	Front/side-rear/side
4				1.0	0.01	0.01	$\boxed{0.33}$	front-rear
5					1.0	0.20	0.09	
6						1.0	−0.04	
7							1.0	

Table 1. Correlation coefficient matrix for the maximum common information (MCI) data set.

IMAGE	1	2	3	4	5	6	7	
1	1.00	0.27	0.24	0.10	0.28	0.17	0.07	
2		1.00	0.17	−0.02	0.16	0.26	0.06	
3			1.00	0.04	$\boxed{0.10}$	0.47	0.17	Front/side-rear/side
4				1.00	0.00	−0.01	$\boxed{0.12}$	front/rear
5					1.00	0.20	0.05	
6						1.00	0.00	
7							1.00	

Table 2. Correlation coefficient matrix for the centroid data set.

To further pursue these image structure and high intensity features of the MCI filter, we form the correlation coefficient matrices of both image sets (Tables 1 and 2). We denote the elements of these matrices by r'_{ij} and note that they are the elements r_{ij} of the corresponding autocorrelation matrix normalized by the square root of the product of the energies of each input image pair. These r'_{ij} are thus measures of the common structure present between different input image pairs. If the structures in images i and j are identical, then $r'_{ij} = 1$ (autocorrelation). As their structures differ, r'_{ij} decreases. In comparing Tables 1 and 2, we note that different image pairs exhibit a larger increase due to MCI than do others. The F/S-R/S and the F-R image pair cross-correlations are boxed for comparison in Tables 1 and 2. These image pairs show large (2.9 to 5.0) improvement gain factors. This is expected because these image pairs have significant common structure (as an inspection of the images will confirm).

Our major concern is that this structural alignment occurs automatically without the need to use merely ad hoc techniques. Moreso, the structural alignment in an MCI filter is weighted by the energies of each of the aligned image parts. To quantify the discrimination ability of the MCI SDF filter, we use the reduced set of two tank images, f_1 (RS, right side) and f_2 (R/S, rear/side) as shown in Figures 3a and 3b. The autocorrelation matrix, G-S coefficient matrix, target matrix and inverse target matrix for these data were then formed (Figure 4). From this, the SDF

$$\hat{h}' = \hat{f}_1 + 0.46\hat{f}_2 \tag{15}$$

was determined using $R_p = 1$. The correlation of this filter with the inputs f_1 and f_5 gave equal output correlation values of $R_p = 30.3$. We then correlated this same SDF filter with a typical false target, an armored personnel carrier (APC) shown in Figure 3c. For this cross-correlation, we found a much lower correlation peak intensity value of 5.4 (or 7dB below the true target correlations). We thus conclude that the discrimination performance of the MCI SDF filter is quite good as predicted.

Casasent 5

3a 3b 3c

FIGURE 3. Photographs of two tank targets. (a) f_1, RS (right side), (b) f_5, R/S (rear/side) and a false target (c) f_f (armored personnel carrier).

$$\begin{array}{c|cc} & f_1 & f_5 \\ \hline f_1 & 8.79 & 1.94 \\ f_5 & 1.94 & 18.9 \end{array}$$

4a

$$\begin{array}{c|cc} & f_1 & f_5 \\ \hline \emptyset_1 & 0.33 & 0.00 \\ \emptyset_2 & -0.05 & 0.23 \end{array}$$

4b

$$\begin{array}{c|cc} & \emptyset_1 & \emptyset_2 \\ \hline f_1 & 2.96 & 0.00 \\ f_5 & 0.21 & 4.31 \end{array}$$

4c

$$\begin{array}{|cc} 0.33 & 0.00 \\ -0.01 & 0.23 \end{array}$$

4d

FIGURE 4. Data matrices for the imagery in Figures 3a and 3b. (a) Auto-correlation matrix, (b) G-S coefficient matrix, (c) Target matrix $\underline{F}_T$, and (d) Inverse target matrix $\underline{F}_T^{-1}$.

5. DISCRIMINATION USING MULTI-CHANNEL SDFs AND NON-UNITARY TRANSFORMATIONS

Conventional unitary transformations do not yield a different effective $\hat{h}$ filter function and hence no reduction in the volume of the discriminant surface will occur. Moreso, only quite restricted discriminant surfaces (i.e. a hyperplane or a hypersphere) are possible with one unitary transformation. In this section, we highlight our recent work on the use of non-unitary transformations for multi-channel SDF processors to provide hyperspace discriminant surfaces of more complex shape and with fewer points on them. This should yield better discrimination performance for the SDF system. This technique is of considerable use in the case of low energy false targets that lie within the neighborhood of the original discriminant hyperplane described by (4). Elimination of such noise or false targets f_f requires a hyperspace discriminant surface of reduce area (or volume). Only non-unitary transformations can achieve this (since the filter function $\hat{h}$ is effectively the same, but in a rotated hyperspace, for the case of unitary transformations) and a multi-channel SDF system is necessary.

Specifically, we envision an input target set $\{f_t\}$ with a SDF filter $\hat{h}$. Applying a non-unitary transformation T to $\{f_t\}$ we obtain a new data set $\{f_T\}$ and a new $\hat{h}_T$ filter. If we require $\{f_t\}$ to satisfy $\hat{h}$ and $\{f_T\}$ to satisfy $\hat{h}_T$, then only a reduced class of inputs will solve both filter functions. This occurs because the non-unitary transformations yield new inputs not present in the original set of data. The resultant intersection of the discriminant hypersurfaces for both filters (one will be a hyperplane and the other of more complex shape) will be a more complex surface with fewer vector points included. Thus, fewer input images will satisfy this processor and improved discrimination will result. We have considered two such non-unitary transformations, the normalization of targets $f_T(x,\tau) = f(x)/\epsilon_f$ and the square-law transformation $f_T(x) = f^2(x)$.

Casasent 6

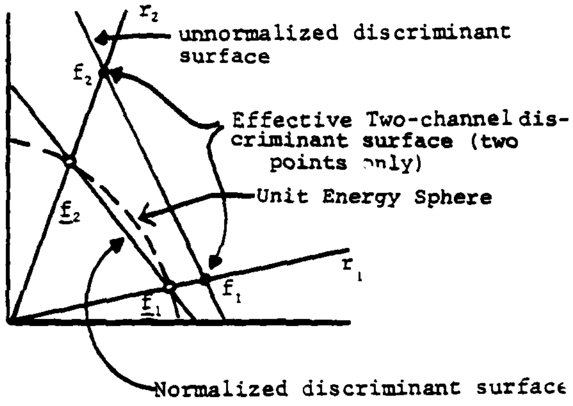
r_2
unnormalized discriminant surface
f_2
Effective Two-channel discriminant surface (two points only)
$\underline{f}_2$
Unit Energy Sphere
r_1
f_1
$\underline{f}_1$
Normalized discriminant surface

FIGURE 5. Multi-channel SDF processor using a non-unitary normalization transformation. The common discriminant hypersurface is the points f_1 and f_2.

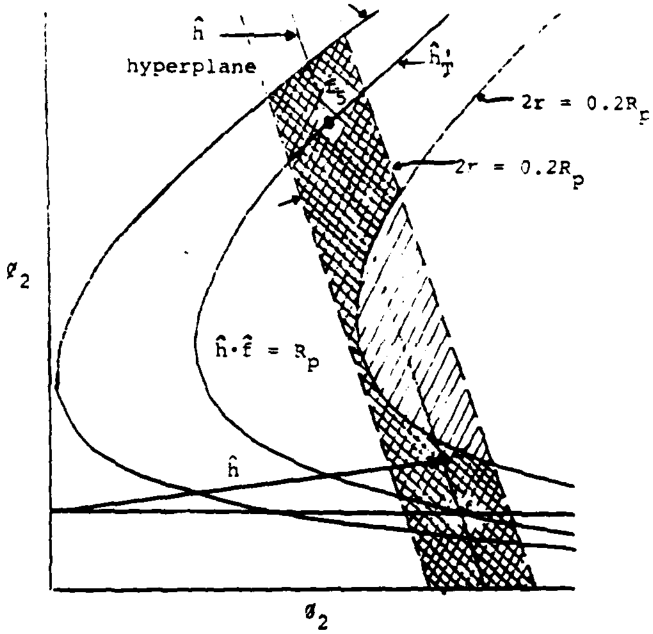

FIGURE 6. Multi-channel SDF processor using a non-unitary square-law transformation. With $R_p = R_p \pm 0.1R_p$, the common discriminant hypersurface is the double cross-hatched region shown.

In Figures 5 and 6, we show the intersection of these two multi-channel discriminant surfaces. The second surface, produced by the non-unitary transformation is not a plane. In the case of the normalized transformation (Figure 5), it is the unit equi-energy (normalized intensity) sphere. In this case (with no noise), the discriminant surface is simply two points corresponding to the two input target data set assumed. In the second case (Figure 6), the square-law transformation corresponds to a hyperspace that is a parabola in the original basis space. The resultant discriminant surface (using an $R_p \pm 0.1R_p$ threshold on the value of the output correlation) is shown by the double cross-hatched area in Figure 6. In both cases, the intersection volume of the discriminant surface is reducedand false targets of low energy and those false targets lying close to the original discriminant hyperplane will not be recognized in this new multi-channel system.

6. NON-UNITARY DECORRELATION TRANSFORMATION FOR IMPROVED DISCRIMINATION

As noted in Sections 4 and 5, only non-unitary transformations can change the effective hyperspace representation of a given data set. From our correlation plane SNR analysis and our hyperspace description (Section 2) of the SDF correlator, we see that a reduced hyperspace area or volume leads to a pattern recognition system with better discrimination. Thus, in this section, we consider use of a new decorrelation transformation that can be applied to a G-S or a K-L image basis set to remove selected basis functions and hence selected inputs. This operation thereby decreases the dimensionality of the hyperspace and thus improves the discrimination performance of the processor by removing false target and noise data. For our experiments, we chose a G-S basis set since the basis function ϕ_m in this representation is a function of the input f_m alone. In a K-L basis set, each ϕ_{KL} is a function of all of the input images. Thus, a G-S representation is more conducive for direct use of our proposed non-unitary transformation, since it directly removes selected basis functions and hence selected inputs (e.g. false targets f_f). A K-L basis set representation is of utmost use in reducing the dimensionality of the data. Techniques to obtain separate K-L basis functions corresponding to two different classes of inputs have been advanced [9] and are appropriate in advanced versions of our decorrelation transformation. Lack of a sufficiently large statistical ensemble of true f_t and false f_f target data precluded use of this K-L transformation in our present experiments.

Our proposed non-unitary decorrelation transformation concept is quite simple. We describe it for a simple case and then extend the concept to the more general problem. We

302-27

assume that the first basis function ϕ_1 corresponds to a false target f_f (in the G-S technique, this is easily achieved by picking $f_1 = f_f$) and that the remaining $N - 1$ basis functions correspond to true targets f_t (i.e., in the G-S technique, we select f_2-f_N to be members of $\{f_t\}$). We apply the non-unitary decorrelation transformation $\underline{\mu}$ to the target matrix $\underline{F}_T$ to obtain a new target matrix $\underline{F}_T'$ as below

$$\underline{F}_T\underline{\mu} = \begin{bmatrix} \hat{f}_1 \\ \cdot \\ \cdot \\ \cdot \\ \hat{f}_N \end{bmatrix} \begin{bmatrix} 0_1 & & \bigcirc \\ & \ddots & \\ \bigcirc & & 1 \end{bmatrix} = \begin{bmatrix} 0 & & & \\ 0 & a_{22} & & \bigcirc \\ \cdot & & \ddots & \\ \cdot & & & \ddots \\ 0 & a_{N2} & \cdots & a_{NM} \end{bmatrix} = \underline{F}_T'. \qquad (16)$$

From (16), we see that the decorrelation transformation $\underline{\mu}$ has yielded a new target matrix with all information associated with the first basis function ϕ_1 (and hence the false target input $f_1 = f_f$) removed. The new $\hat{h}'$ calculated from this $\underline{F}_T'$ will thus not contain any of the false target energy associated with $\hat{f}_1 = \hat{f}_f$. Its performance and discrimination will thus be improved. We can directly extend this technique to larger $\{f_f\}$ data sets by letting the first J input functions $f_1 \longrightarrow f_J$ in $\{f_n\}$ in the G-S procedure correspond to $\{f_f\}$ and the last $N - J$ elements correspond to $\{f_t\}$. K-L techniques [9] can also be developed to produce separate basis functions corresponding to different image classes. (In this case, a greatly reduced dimensionality is sufficient to represent the true and false target data sets).

$$\begin{array}{c|ccc} & f_f & f_1 & f_5 \\ \hline f_f & 2.68 & 0.54 & 0.91 \\ f_1 & 0.54 & 8.79 & 1.94 \\ f_5 & 0.91 & 1.94 & 18.9 \end{array} \qquad \begin{array}{c|ccc} & f_f & f_1 & f_5 \\ \hline \phi_1 & 0.61 & 0 & 0 \\ \phi_2 & -0.06 & 0.33 & 0 \\ \phi_3 & -0.07 & -0.04 & 0.23 \end{array} \qquad \begin{array}{c|ccc} & \phi_1 & \phi_2 & \phi_3 \\ \hline f_f & 1.63 & 0 & 0 \\ f_1 & 0.32 & 2.98 & 0 \\ f_5 & 0.54 & 0.05 & 4.26 \end{array} \qquad \begin{array}{c|cc} & \phi_2 & \phi_3 \\ \hline f_1 & 2.98 & 0 \\ & & \\ f_5 & 0.05 & 4.26 \end{array} \qquad \begin{array}{|cc} \hline 54.6 & 0 \\ & \\ -0.69 & 38.2 \end{array}$$

(7a) (7b) (7c) (7d) (7e)

FIGURE 7. Data matrices for the decorrelation transformation on the data of Figure 3. (a) Auto-correlation matrix, (b) G-S coefficient matrix, (c) Full target matrix $\underline{F}_T$, (d) reduced target matrix $\underline{F}_T'$, and (e) inverse of reduced target matrix $\underline{F}_T'^{-1}$.

To demonstrate the use of this technique, we return to the examples in Figures 3 and 4. We use the APC (Figure 3c) as f_f (our first function) and the two tank images (Figures 3a and 3b) as our second and third input functions. In Figure 7, we show the autocorrelation matrix, G-S coefficient matrix, full target matrix $\underline{F}_T$, reduced target matrix $\underline{F}_T'$, and the inverse $\underline{F}_T'^{-1}$ of the reduced target matrix for these inputs. The reduced target matrix $\underline{F}_T'$ is obtained by applying

$$\underline{\mu} = \begin{bmatrix} 0 & 0 & 0 \\ 0 & 1 & 0 \\ 0 & 0 & 1 \end{bmatrix} \qquad (17)$$

to $\underline{F}_T$. It thus consists of the lower two rows and columns of $\underline{F}_T$. The new filter computed from this $\underline{F}_T'$ is

$$\hat{h}' = \hat{f}_1 + 0.42\,\hat{f}_5 - 0.10\,\hat{f}_f. \qquad (18)$$

This new filter function was calculated, synthesized and correlated with the $\hat{f}_1$, $\hat{f}_5$ and $\hat{f}_f$ inputs. When applied to the true target inputs ($\hat{f}_1$ and $\hat{f}_5$), an $R_p = 30.0$ value was obtained. This represents only a negligible 1% loss from the $R_p = 30.3$ value obtained in Section 4. For the cross-correlation of $\hat{h}'$ with the false target $\hat{f}_f$, $R_p = 0$ was obtained at $\tau = 0$. We can widen the null in the $\hat{f}_f \cdot \hat{h}'$ correlation output by using more f_f inputs (each being a shifted version of the $\hat{f}_f$ false target used). For our case, five such inputs would suffice to null all shifted versions of $\hat{f}_f$.

7. SUMMARY AND CONCLUSIONS

In this paper, we have reviewed our hyperspace description of a matched spatial filter (MSF) correlator, the concept of the use of a synthetic discriminant function (SDF) as the MSF reference and several techniques for generating the basis function sets necessary to obtain the SDF. As before, bandpass filter preprocessing is used to remove the effects

Casasent 8

of intensity differences in the data (a problem that arises with IR and multisensor imagery). A maximum common information (MCI) filter concept used to maintain intra-class recognition of different aspect views of the reference object with one MCI SDF filter was analyzed for its ability to also perform inter-class discrimination between true and false targets. The structure and intensity of the MCI SDF was found to be excellent and its ability to suppress false target correlations was measured and seen to be good.

Non-unitary transformations to produce hypersurfaces with a reduced number of data points and with more complex shapes were then described. A multi-channel SDF system was shown to be quite useful. Two examples of such systems were discussed. A new decorrelation transformation was then presented that allowed specific false targets (or colored background noise of non-zero mean) to be eliminated from the data set. Experimental verification on IR imagery of different aspect views of an M-60 tank and an armored personnel carrier false target were obtained with excellent results.

The advanced discrimination techniques described and demonstrated in this paper make the use of SDFs in optical or digital MSF correlators even more attractive and practical than they initially were.

ACKNOWLEDGEMENT

The support of the Air Force Office of Scientific Research (Grant 79-0091) for the research reported in this paper is gratefully acknowledged. The support of C.F.H. by the U.S. Army Missile Research and Development Command during his stay at Carnegie-Mellon University is also gratefully acknowledged.

REFERENCES

1. Proc IEEE, 67, Special Issue on Pattern Recognition (May 1979).
2. D. Casasent, Proc IEEE, 67, 803 (1979).
3. W. Pratt, Digital Image Processing, Wiley, New York (1978).
4. C. Hester and D. Casasent, SPIE, 302 (1981).
5. D. Casasent and D. Psaltis, Proc IEEE, 65, 77 (1977).
6. C. Hester and D. Casasent, Applied Optics, 19, 1758 (1980).
7. C. Hester and D. Casasent, SPIE, 201, 77 (1979).
8. S. Watanabe, Trans Fourth Prague Conf, C19, 635 (1965).
9. K. Fukunaga and W. Koontz, IEEE, C19, 635 (1970).

8. REFERENCES

1. "A Laser Diode Lensless MSF-HOE Correlator," Applied Optics, 19, 2653-4, August 1980 (Caimi et al).

2. "Lensless Matched Spatial Filter Correlator Experiments," Opt Commun, 34, 311-315, September 1980 (M. Shen et al).

3. "HOE/Lensless Matched Spatial Filter Wavelength-Scaling Correlator," Opt Commun, 34, 316-320, September 1980 (M. Shen et al).

4. "A Laser Diode/Lensless MSF Optical Pattern Recognition System," EOSD, 46-52, November 1980 (Casasent et al).

5. D. Casasent, F. Caimi and A. Khomenko, Applied Optics (15 September 1981).

6. D. Casasent, F. Caimi and A. Khomenko, Applied Optics (submitted 1981).

7. D. Casasent, F. Caimi, M. Petrov and A. Khomenko, Applied Optics (to be submitted).

8. D. Casasent and F. Caimi, EOSD (to be submitted).

9. D. Casasent, S. Eiva and B. Kumar, "Image Quality Effects in Optical Correlators," SPIE, 310 (1981).

10. Y. Barniv, H. Mostafavi, and D. Casasent, "Correlation of Images with Random Contrast Reversals," SPIE, 238, 156 (July 1980).

11. Y. Barniv and D. Casasent, "Multisensor Image Registration: Experimental Verification," SPIE, 292 (August 1981).

12. C. Hester and D. Casasent, "Multivariant Technique for Multiclass Pattern Recognition," Applied Optics, 19, 1758 (June 1980).

13. C. Hester and D. Casasent, "Intra-Class IR Tank Pattern Recognition Using SDFs," SPIE, 292 (August 1981).

14. C. Hester and D. Casasent, "Inter-Class Discrimination Using SDFs," SPIE, 302 (August 1981).

15. "An Iterative Color Multiplexed Electro-Optical Processor," Opt Lett, 4, 348-350, November 1979 (Psaltis, Casasent and Carlotto).

16. D. Casasent and C. Neuman, NASA Langley Conference (to appear).

17. D. Casasent, C. Neuman and M. Carlotto, "An Electro-Optical Processor for Optimal Control," SPIE, 295 (August 1981).

18. M. Carlotto and D. Casasent, "An Iterative Optical Vector-Matrix Processor," SPIE Institute Series, (submitted 1981).

19. M. Carlotto and D. Casasent, "A Microprocessor-Based Fiber-Optic Iterative Optical Processor," Applied Optics (submitted 1981).

20. "Optical Pattern Recognition: Matched Spatial Filter Processors," *EOSD*, (November 1980), 33-39 (Casasent).

21. "Optical Pattern Recognition: Beyond Matched Spatial Filtering," *EOSD*, March 1981, 39-47 (Casasent).

22. "Pattern Recognition: A Review," *IEEE Spectrum*, 28-33, March 1981 (Casasent).

23. "Processing Flexibility by Hybrid Optical/Digital Techniques," Proc. Workshop of Future Directions in Optical Data Processing, Texas Tech. Rept., 1 March 1981, 1723 (Casasent and Kumar).

9. PUBLICATIONS

9.1 PUBLICATIONS (FY 1982)

Publications from 1 September 1980 - 1 September 1981 on work performed under AFOSR-79-0091 follow.

9.1.1 PAPERS PUBLISHED

1. "Hybrid Processor to Compute Invariant Moments for Pattern Recognition," Opt Lett, 5, 395-7, September 1980 (Casasent and Psaltis).
2. "Optical Work Recognition, Case Study in Coherent Optical Pattern Recognition," Opt Engr, 19, 716-721, September 1980 (Casasent et al).
3. "Lensless Matched Spatial Filter Correlator Experiments," Opt Commun, 34, 311-315, September 1980 (M. Shen et al).
4. "HOE/Lensless Matched Spatial Filter Wavelength-Scaling Correlator," Opt Commun, 34, 316-320, September 1980 (M. Shen et al).
5. "A Laser Diode/Lensless MSF Optical Pattern Recognition System," EOSD, 46-52, November 1980 (Casasent et al).
6. "Optical Pattern Recognition: Matched Spatial Filter Processors," EOSD, November 1980, 33-39 (Casasent).
7. "Optical Pattern Recognition: Beyond Matched Spatial Filtering," EOSD, March 1981, 39-47 (Casasent).
8. "Pattern Recognition: A Review," IEEE Spectrum, 28-33, March 1981 (Casasent).
9. "Processing Flexibility by Hybrid Optical/Digital Techniques," Proc. Workshop of Future Directions in Optical Data Processing, Texas Tech. Rept., 1 March 1981, 17-23 (Casasent and Kumar).
10. "Binarization Effects in a Correlator with Noisy Input Data," Appl Opt, 20, 1433-1438, April 1981 (Kumar and Casasent).
11. "Beyond Matched Filtering," Israel J. Techn (Accepted) (Casasent).
12. "A Laser Diode/HOE Pattern Recognition System," Academia Sinica, (Accepted) (Casasent).
13. Y. Barniv, H. Mostafavi and D. Casasent, "Correlation of Images with Random Contrast Reversals," SPIE, 238, 156 (July 1980).

14. D. Casasent, S. Eiva and B. Kumar, "Image Quality Effects in Optical Correlators," SPIE, 310 (August 1981).
15. Y. Barniv and D. Casasent, "Multisensor Image Registration: Experimental Verification," SPIE, 292 (August 1981).
16. C. Hester and D. Casasent, "Intra-Class IR Tank Pattern Recognition Using SDFs," SPIE, 292, (August 1981).
17. C. Hester and D. Casasent, "Inter-Class Discrimination Using SDFs," SPIE, 302 (August 1981).

9.1.2 PAPERS SUBMITTED

18. "Input Quantization Effects in an Image Correlator," Appl Opt, Submitted (Kumar and Casasent).
19. D. Casasent, F. Caimi and A. Khomenko, "The Soviet Priz Spatial Light Modulator," Applied Optics, Rapid Communications (accepted 1981).
20. D. Casasent, F. Caimi and A. Khomenko, "Test and Evaluation of the Soviet Prom and Priz Spatial Light Modulators," Applied Optics (submitted 1981).
21. D. Casasent and C. Neuman, "An Iterative Optical Processor: Selective Survey of Operations Achievable," Proceedings NASA Langley Conference on Optical Information Processing (August 1981).
22. M. Carlotto and D. Casasent, "An Iterative Optical Vector-Matrix Processor," SPIE Institute Series, (submitted 1981).
23. M. Carlotto and D. Casasent, "A Microprocessor-Based Fiber-Optic Iterative Optical Processor," Applied Optics (submitted 1981).

9.2 SEMINARS AND PRESENTATIONS (1 October 1980 - 31 September 1981)

1. "Optical Data Processing", Carnegie-Mellon University, Sophomore Seminar, (October 1980).
2. "Airborne Optical Pattern Recognition System Design", EOSD Conference, Boston (November 1980).
3. "Optical Pattern Recognition", General Dynamics, Pomona, California (December 1980).
4. "Optical Pattern Recognition", Northrop Corporation, Anaheim, California (December 1980).

5. "Optical Pattern Recognition", Hughes Research Corporation, Malibu, California (December 1980).

6. "Optical Pattern Recognition", BDM Corporation, Virginia (February 1981).

7. "Optical Vector-Matrix Processors," Washington, D.C., NRL 2-D Signal Processing Conference, (March 1981).

8. "Optical Pattern Recognition", Eglin Air Force Base, Florida (March 1981).

9. "Optical Pattern Recognition", Ball Aerospace Corporation, Boulder, Colorado, (March 1981).

10. "Optical Data Processing", CMU, Pittsburgh, Management Program (April 1981).

11. "Optical Data Processing at CMU", OSA Meeting, Pittsburgh (April 1981).

12. "Optical Processors for Robotics Applications", Westinghouse Corporation, Pittsburgh (May 1981).

13. "Optical Processors for Robotics Applications", CMU, Pittsburgh (May 1981).

14. "Use of Synthetic Discriminant Functions in Optical Pattern Recognition", General Dynamics, Pomona, California (August 1981).

15. "Design of and Operations Achievable on an Iterative Optical Processor", Anaheim, California (August 1981).

16. "Operations Achievable on an Iterative Optical Vector-Matrix Processor", NASA Conference on Optical Information Processing for Aerospace Applications, NASA Langley, Virginia (August 1981).

17. "Optical Pattern Recognition for Missile Guidance", General Dynamics, Convair Division, San Diego, California (August 1981).

18. "Optical Pattern Recognition for Industrial Applications", TRW Corporation, Los Angeles, California (August 1981).

19. "Intra-Class Pattern Recognition Using Synthetic Discriminant Functions", SPIE Conference, San Diego, California (August 1981).

20. "Inter-Class Discrimination Using Synthetic Discriminant Functions", SPIE Conference, San Diego, California (August 1981).

21. "Multi-Sensor Optical Pattern Recognition: Experimental Verification", SPIE Conference, SPIE, San Diego, California (August 1981).

22. "Image Quality Effects on Optical Pattern Recognition", SPIE Conference, San Diego, California (August 1981).

23. "Optical Information Processing at CMU in EE", CMU, Pittsburgh, Sophomore Seminar (September 1981).

9.3 THESES SUPPORTED BY AFOSR (October 1980 - September 1981)

1. Hiroyasu Murakami, M.S. Dissertation, "Matched Filter Statistical Correlator" (February 1981).
2. Saulius Eiva, M.S. Dissertation, "Image Quality Effects in Optical Correlators" (May 1981).
3. C. Hester Ph.D. Dissertation, "Synthetic Filters for Multiclass Pattern Recognition" (May 1981).
4. Y. Barniv, Ph.D. Dissertation, "Multi-Sensor Image Registration" (May 1981).
5. M. Carlotto, Ph.D. Dissertation, "Iterative Electro-Optic Matrix Processor" (May 1981).
6. A. Sexton, M.S. Dissertation, "Digital Analysis of Space-Variant Optical Processors" (July 1981).

9.4 PATENTS (1 October 1980 - 31 September 1981)

Four patent disclosures were produced during the past year. The titles of these follow.

(1) Multiple-Invariant Space-Variant Pattern Recognition System,

(2) Pattern Recognition by Invariant Moments,

(3) Synthetic-Discriminant Functions for Multi-Class Pattern Recognition,

(4) Equalization and Coherence Measure Correlator.

A patent has been submitted on item (3) above.

AF invention number 14,509 "Multi-Variant Technique for Multi-Class Pattern Recognition."

9.5 PUBLICATIONS TO DATE (1 October 1979 - 30 September 1981)

Publications on research sponsored by AFOSR-79-0091 grant (1 October 1979 - 30 September 1980) follow. The FY81 list of publications is contained in Section 9.1.

1. "Photo-DKDP Light Valve in Optical Data Processing," Appl Opt, 18, 3307-3314, October 1979 (Casasent and Luu).
2. "Coherent Optical Pattern Recognition," Nikkei Electronics, 150-181, October 1979, In Japanese (Casasent).
3. "Optical Data Processing for Advanced Missile Guidance Needs," AIAA, October 1979 (Casasent).
4. "Spread Spectrum Optical Signal Processors," Proc EOSD, 333-342, October 1979, (Casasent and Psaltis).
5. "Space Blue Bandwidth Product in Correlator Performance Evaluation," J Opt Soc Amer, 70, 103-110, January 1980, (Kumar and Casasent).
6. "Optical Image Processing," EOSD, Tokyo, January 1980, In Japanese (Casasent).
7. "Optical Signal Processing," EOSD, Tokyo, January 1980, In Japanese (Casasent).
8. "Beyond Matched Filtering," Opt Engr, 19, 152-156, (March 1980) February 1980 (Caulfield et al).
9. "Multivariant Technique for Multi-Class Pattern Recognition," Appl Opt, 19, 1758-1761, June 1980 (Hester and Casasent).
10. "Optical Fourier Transform Techniques for Advanced Fourier Spectroscopy," Appl Opt, 19, 2034-2037, June 1980 (Casasent and Psaltis).
11. "Non-Linear t-E Curve Effects in an Optical Correlator," Opt Comm, 34, 4-6, July 1980 (Kumar and Casasent).
12. "Correlation of Images with Random Contrast Reversals," SPIE, 238, 156-165, July 1980 (Barniv, Mostafavi, Casasent).
13. "A Laser Diode Lensless MSF-HOE Correlator," Appl Opt, 19, 2653-2654, August 1980 (Caimi et al).